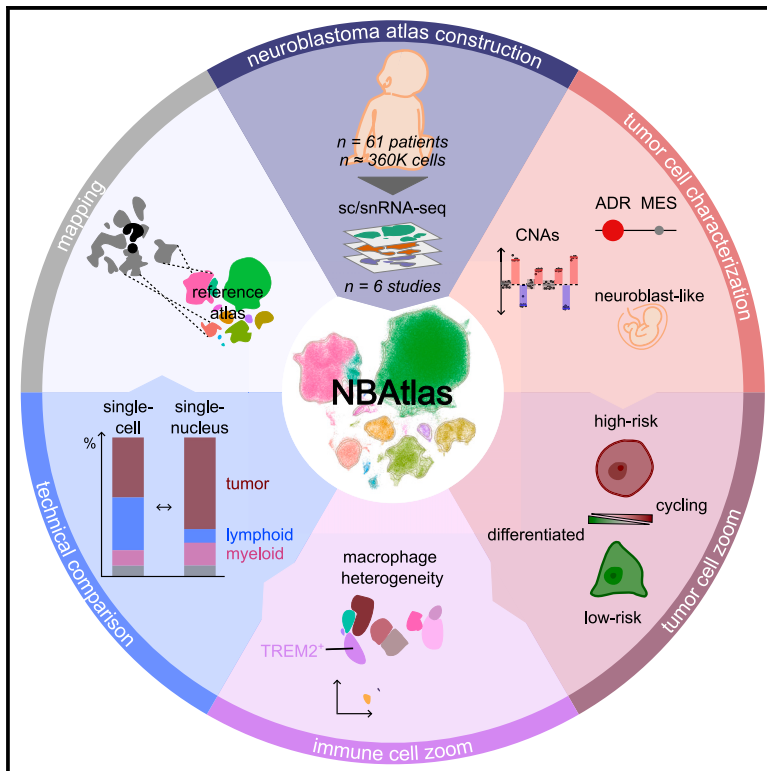


# NBATlas: A harmonized single-cell transcriptomic reference atlas of human neuroblastoma tumors

## Graphical abstract



## Authors

Noah Bonine, Vittorio Zanzani, Annelies Van Hemelryk, ..., Vanessa Vermeirssen, Charlotte L. Scott, Katleen De Preter

## Correspondence

charlotte.scott@irc.vib-ugent.be (C.L.S.), katleen.depreter@ugent.be (K.D.P.)

## In brief

Bonine et al. integrate neuroblastoma tumor single-cell/nucleus RNA-sequencing data from 61 patients into “NBAtlas,” further unraveling the transcriptional landscape of neuroblastoma as well as highlighting some technical challenges. This resource will aid future single-cell investigations.

## Highlights

- The NBAtlas includes single-cell/nucleus RNA-seq data from 61 neuroblastoma patients
- Malignant neuroendocrine cells comprise cycling high-risk vs. differentiated low-risk cells
- Macrophage heterogeneity is considerable and includes high-risk-associated TREM2<sup>+</sup>-cells
- The NBAtlas enables accurate reference-based mapping of new data



## Resource

# NBAtlas: A harmonized single-cell transcriptomic reference atlas of human neuroblastoma tumors

Noah Bonine,<sup>1,2,3</sup> Vittorio Zanzani,<sup>1,2,3,4,8,11</sup> Annelies Van Hemelryk,<sup>1,3,4,5,11</sup> Bavo Vanneste,<sup>4,5</sup> Christian Zwicker,<sup>4,5</sup> Tinne Thoné,<sup>4,5</sup> Sofie Roelandt,<sup>1,2,3</sup> Sarah-Lee Bekaert,<sup>1,3</sup> Jan Koster,<sup>6</sup> Isabelle Janoueix-Lerosey,<sup>7</sup> Cécile Thirant,<sup>7</sup> Stéphane Van Haver,<sup>1,3,9</sup> Stephen S. Roberts,<sup>10</sup> Liselot M. Mus,<sup>1,3</sup> Bram De Wilde,<sup>1,3</sup> Nadine Van Roy,<sup>1,3</sup> Celine Everaert,<sup>1,2,3</sup> Frank Speleman,<sup>1,3</sup> Vanessa Vermeirssen,<sup>1,3,4,8</sup> Charlotte L. Scott,<sup>4,5,12,\*</sup> and Katleen De Preter<sup>1,2,3,12,13,\*</sup>

<sup>1</sup>Department of Biomolecular Medicine, Ghent University, Ghent, Belgium

<sup>2</sup>VIB-UGent Center for Medical Biotechnology, Ghent University, Ghent, Belgium

<sup>3</sup>Cancer Research Institute Ghent (CRIG), Ghent, Belgium

<sup>4</sup>Department of Biomedical Molecular Biology, Ghent University, Ghent, Belgium

<sup>5</sup>Laboratory of Myeloid Cell Biology in Tissue Damage and Inflammation, VIB-UGent Center for Inflammation Research, Technologiepark-Zwijnaarde 71, 9052 Ghent, Belgium

<sup>6</sup>Amsterdam UMC Location University of Amsterdam, Center for Experimental and Molecular Medicine, Cancer Center Amsterdam, Amsterdam, the Netherlands

<sup>7</sup>Inserm U830, Diversity and Plasticity of Childhood Tumors Lab, PSL Research University, Institut Curie Research Center, Paris, France

<sup>8</sup>Laboratory for Computational Biology, Integromics and Gene Regulation (CBIGR), Ghent University, Ghent, Belgium

<sup>9</sup>Tow Center for Developmental Oncology, Department of Pediatrics, Memorial Sloan Kettering Cancer Center, New York, NY, USA

<sup>10</sup>Department of Pediatrics, Oregon Health & Science University, Portland, OR, USA

<sup>11</sup>These authors contributed equally

<sup>12</sup>These authors contributed equally

<sup>13</sup>Lead contact

\*Correspondence: [charlotte.scott@irc.vib-ugent.be](mailto:charlotte.scott@irc.vib-ugent.be) (C.L.S.), [katleen.depreter@ugent.be](mailto:katleen.depreter@ugent.be) (K.D.P.)

<https://doi.org/10.1016/j.celrep.2024.114804>

## SUMMARY

Neuroblastoma, a rare embryonic tumor arising from neural crest development, is responsible for 15% of pediatric cancer-related deaths. Recently, several single-cell transcriptome studies were performed on neuroblastoma patient samples to investigate the cell of origin and tumor heterogeneity. However, these individual studies involved a small number of tumors and cells, limiting the conclusions that could be drawn. To overcome this limitation, we integrated seven single-cell or single-nucleus datasets into a harmonized cell atlas covering 362,991 cells across 61 patients. We use this atlas to decipher the transcriptional landscape of neuroblastoma at single-cell resolution, revealing associations between transcriptomic profiles and clinical outcomes within the tumor compartment. In addition, we characterize the complex immune-cell landscape and uncover considerable heterogeneity among tumor-associated macrophages. Finally, we showcase the utility of our atlas as a resource by expanding it with additional data and using it as a reference for data-driven cell-type annotation.

## INTRODUCTION

Neuroblastoma is the most common extracranial solid tumor in children.<sup>1</sup> The tumor cells arise from undifferentiated migratory neural crest cells during early fetal development.<sup>2</sup> Most tumors that emerge before the age of 18 months show genomes marked by recurrent patterns of whole-chromosome gains and losses. These low-risk tumors have an excellent prognosis. However, the prognosis in older children is less favorable. Here, three major genetic subtypes are discerned: tumors with (1) *MYCN* amplification, (2) hTERT activation, or (3) alternative lengthening of telomeres.<sup>3,4</sup> These three classes of high-risk tumors are marked by recurrent patterns of copy-number alterations (CNAs) including 17q gains and 1p losses. Contrary to CNAs, gene mu-

tations are not as common except for activating *ALK* mutations, which occur as somatic events across all tumor subtypes and as germline events that cause familial neuroblastoma in rare cases.<sup>5,6</sup> Of note, *ALK* mutations and RAS/MAPK-pathway mutations are enriched in relapsed neuroblastoma.<sup>7–9</sup>

Despite very intensive multimodal therapy including chemotherapy, radiation, stem cell transplantation, and immunotherapy, nearly half of all high-risk patients relapse and succumb to the disease, while survivors often suffer from long-term therapy-related toxicity.<sup>1,10</sup> Moreover, the implementation of immunotherapy has been challenging, since neuroblastomas, especially in high-risk patients, are considered immunologically “cold” tumors, presenting with only limited lymphocyte infiltration.<sup>11</sup> Despite this, progress has been made, as the





tumor-specific surface molecule GD2 can be targeted with monoclonal antibodies, an immunotherapy now included in the standard of care for high-risk patients.<sup>12,13</sup> In addition, anti-GD2 chimeric antigen receptor T cell therapy shows promising results in clinical trials,<sup>14</sup> thus demonstrating the potential impact of targeting the immune system in neuroblastoma.

Recent advances in single-cell transcriptomics have greatly improved our understanding of the cellular composition of different healthy and diseased tissues. Over the past few years, several transcriptomic datasets of neuroblastoma patient samples at single-cell level have been published.<sup>15–23</sup> These foundational studies have provided deeper insights into the enigmatic cellular heterogeneity, tumor microenvironment (TME), and origins of neuroblastoma tumors. All studies find adrenergic (also termed noradrenergic) tumor cells, while only some provide potential clues of plasticity toward malignant mesenchymal cells.<sup>21,23</sup> Also, by comparison to normal development, these studies collectively identify neuroblasts (also termed sympathoblasts) as the cell of origin for neuroblastoma.<sup>24–27</sup> Finally, the immune microenvironment of neuroblastoma tumors has also been explored, indicating (sub)populations linked to survival<sup>20</sup> and demonstrating an immunocompromised microenvironment.<sup>18</sup> However, due to the rare occurrence of neuroblastoma, challenging pediatric surgeries, and the high cost of single-cell sequencing experiments, most of these studies only included limited patient numbers (under 20 patients per study). Integration of data from different single-cell datasets allows the generation of comprehensive cell atlases, which further expand our knowledge by assimilating information not captured in individual studies. Moreover, aligning different studies for a specific tissue has several advantages. Among others, it allows for comprehensive charting of the different cell types and subpopulations present in that tissue, facilitates the discovery of novel cell subsets and/or activation states, enables the identification of robust marker genes across studies, and supports the annotation of new datasets by guided cell-type prediction.<sup>28–33</sup> For example, some of the single-cell studies published to date have examined myeloid immune-cell heterogeneity as a potential key player in neuroblastoma pathology.<sup>18,20</sup> However, there is limited overlap in the subsets/states of these cells described, highlighting the need for a more integrated analysis of these cells.

Here, we present a meta-analysis of published neuroblastoma single-cell and single-nucleus RNA datasets that are integrated into a harmonized single-cell transcriptomic atlas we term “NBAtlas” (neuroblastoma atlas). Using this atlas, we comprehensively investigate the transcriptomic heterogeneity of neuroblastoma. From the integrated dataset, we infer CNAs and explore different transcriptomic signatures to discern malignant cells. We link transcriptomic profiles of the tumor compartment to clinical outcomes. Furthermore, we characterize the different immune-cell types within the tumor and the TME, revealing sig-

nificant heterogeneity within the tumor-associated macrophage compartment. We also reveal key technical differences in single-cell and single-nucleus transcriptomic datasets. Finally, we demonstrate the utility of the atlas for integration and annotation of additional data.

## RESULTS

### The NBAtlas is a harmonized single-cell transcriptomic atlas of neuroblastoma tumors

To generate an integrated single-cell atlas of human neuroblastoma tumors, we collected data from seven different single-cell or single-nucleus RNA sequencing (RNA-seq) datasets (originating from six publications).<sup>15–20</sup> This amounted to 68 samples from 61 neuroblastoma patients with different clinical characteristics (Figures 1A and S1A; Table S1). Overall, the integrated dataset includes 42 primary pre-treatment, 10 post-treatment, and 12 relapsed samples (and 4 unknown), with 45 samples originating from high-risk patients and 23 from low- to intermediate-risk patients. Following quality control (see STAR Methods), a total number of 362,991 cells were included in the NBAtlas.

After merging the different datasets, the initial cell clustering was mostly driven by the originating dataset and the specific assay (single-cell vs. single-nucleus) used, pointing to the need for an integration strategy that corrects these expected batch effects (Figure S1B). Therefore, integration was performed using scVI, a deep-learning algorithm tailored to the complex integration task at an atlas scale.<sup>34,35</sup> Application of this integration strategy resulted in an scVI latent space where the cells are harmonized across the different datasets, assays, samples, and platforms as visualized in the UMAPs (Figures 1B, S1C, and S1D). Within this harmonized dataset, cells/nuclei specifically cluster per cell type, identified on the basis of their marker and differentially expressed (DE) genes (Figures 1C, 1D, and S1E; Table S2). The largest cluster comprises neuroendocrine cells (67.4%; Figure S1F), marked by high expression of *PHOX2B*, *NXP1*, and *SYT1* and representing the presumed cancer cells (further discussed below). Next to this, different stromal cell types were identified including endothelial cells (*EGFL7*<sup>+</sup>, *EMCN*<sup>+</sup>, *PLVAP*<sup>+</sup>), Schwann cells (*CDH19*<sup>+</sup>, *PLP1*<sup>+</sup>, *PTPRZ1*<sup>+</sup>), and fibroblasts (*COL1A1*<sup>+</sup>, *COL1A2*<sup>+</sup>, *COL3A1*<sup>+</sup>). In addition, various immune-cell populations formed separate clusters, including T cells (*CD3D*<sup>+</sup>, *CD3E*<sup>+</sup>, *CD2*<sup>+</sup>), natural killer (NK) cells (*KLRF1*<sup>+</sup>, *KLRC1*<sup>+</sup>, *XCL2*<sup>+</sup>), B cells (*MS4A1*<sup>+</sup>, *CD79A*<sup>+</sup>, *VPREB3*<sup>+</sup>), plasma cells (*IGHG1*<sup>+</sup>, *IGHG2*<sup>+</sup>, *IGHG3*<sup>+</sup>), myeloid cells (*LYZ*<sup>+</sup>, *IL1B*<sup>+</sup>, *C1QC*<sup>+</sup>), and plasmacytoid dendritic cells (pDCs; *LILRA4*<sup>+</sup>, *SCT*<sup>+</sup>, *PTCRA*<sup>+</sup>). Finally, we identified two small clusters, one of red blood cells expressing hemoglobin genes (*HBA1*<sup>+</sup>, *HBA2*<sup>+</sup>, *HBB*<sup>+</sup>) and the other expressing adrenal cortex markers (denoted as “stromal other”; *CYP11B1*<sup>+</sup>, *CYP21A2*<sup>+</sup>, *FAM166B*<sup>+</sup>). With the exception of the latter cluster, which was

**Figure 1. NBAtlas: A harmonized single-cell transcriptomic reference atlas of human neuroblastoma tumors**

- (A) Overview of the included datasets.<sup>15–20</sup>  
 (B) UMAP colored according to dataset (top), assay (middle), and sample (bottom).  
 (C) Annotated integrated UMAP of the single cells/nuclei (the rings represent different metadata values per cell type).  
 (D) Expression of key markers used for annotation in (C). NE, neuroendocrine; RBCs, red blood cells.  
 See also Figure S1.

restricted to a few samples, each cell type or group of cell types was represented by cells/nuclei originating from different patients across the various datasets (Figures 1C and S1C). Integration with Harmony<sup>36</sup> showed highly similar results in terms of batch correction and cell-type clustering (Figure S1G).

### Neuroendocrine cells present with molecular hallmarks of malignant neuroblastoma cells

In addition to annotation of the cells/nuclei in the NBAtlas based on cell-type markers or DE genes (Figure 1D), we also applied inferCNV<sup>37</sup> to the single-cell and single-nucleus RNA-seq datasets to infer tumor-specific DNA CNAs in order to distinguish malignant cells from normal stromal and immune-cell types (Figures 2A and S2A). As expected, CNAs were found in neuroendocrine cells while absent in TME cells, including normal fibroblasts and Schwann cells. These included common neuroblastoma-associated CNAs such as 1p-loss and 17q-gain (Figures 2B and S2B). Consistent with this, only neuroendocrine cells were systematically classified as being tumor cells using CopyKAT<sup>17</sup> and SCEVAN,<sup>38</sup> which are tools for CNA inference that distinguish malignant from TME cells (Figure S2C).

At present, while the majority of neuroblastoma tumor cells are assumed to carry an adrenergic identity, work on *in vitro* cultured cells proposes the existence of a second cell state marked by a mesenchymal transcriptional signature, a distinct transcriptional regulatory network, and chemotherapeutic resistance.<sup>39,40</sup> Moreover, under therapeutic pressure, an epigenetic shift of the adrenergic phenotype toward adrenergic cells with immature mesenchymal-like features has been uncovered *in vitro*.<sup>41</sup> Identification of these mesenchymal-like neuroblastoma cells *in vivo*, however, has been challenging and is an area of intensive research.<sup>23,24,42</sup> Given the translational importance, we next investigated signatures for both cell states of neuroblastoma<sup>18–21</sup> in our NBAtlas. For the neuroendocrine cells, the adrenergic signature score is significantly higher compared to the mesenchymal signature score (while the opposite is true for other cells in the TME). Moreover, the mesenchymal signature score is significantly lower in the neuroendocrine cells compared to other cells of the TME without CNAs, with higher expression in mainly endothelial cells, fibroblasts, and Schwann cells (Figures 2C, S2D, and S2E). Taken together, we did not detect a significant contribution of mesenchymal cell identity to the transcriptional heterogeneity in CNA-bearing tumor cells (see also further below).

A major driver of variability in the transcriptomic profiles of neuroendocrine cells appeared to be cell-cycle-phase related (Figure 2D). Proliferating neuroblastoma cells were clearly distinguishable from non-proliferating cells, clustering separately. For these proliferating tumor cells, specific enrichment of replication-stress-associated signatures<sup>43,44</sup> was observed (Figure S2F). Taking this one step further, the expression of a signature associated with prexasertib sensitivity,<sup>44</sup> a drug targeting the replication-stress pathway, was also highly enriched in these proliferating tumor cells, while resistance-associated expression was enriched in other cells (Figure S2G).

Further, to analyze the developmental origin of the neuroendocrine cells, we correlated the expression profiles of these cells to a reference dataset of fetal adrenal medullas<sup>16</sup> using a reference-

based cell annotation (with SingleR and Seurat). Nearly all patient neuroendocrine cells were found to resemble neuroblast populations most closely (Figures 2E, S2H, and S2I). The same analysis of a recently published dataset of a human stem cell model of sympathoadrenal development<sup>45</sup> also resulted in a similar conclusion (Figure S2J).

Thus, overall, neuroendocrine cells show typical characteristics of malignant neuroblastoma tumor cells including CNAs, adrenergic signature expression, and neuroblast-like resemblance.

### Zooming in on malignant cell heterogeneity of neuroblastoma reveals distinct clusters linked to risk groups

To further decipher the heterogeneity of neuroblastoma tumoral cells in patient tumor samples, CNA-bearing neuroendocrine cells (as identified by CopyKAT, Figure S2C) were selected, re-integrated with scVI, and reclustered. This identified seven clusters (denoted as “c”) across the different patients, which were then annotated based on their DE genes and a gene set enrichment analysis (Figures 3A, S3A, and S3B; Table S3). Additional integration with Seurat and ComBat both generated sufficiently batch-corrected embeddings (Figures S3C and S3D). In these embeddings, overall the scVI clusters remained segregated, indicating consistency in biological results (Figures S3C and S3D).

In agreement with the cell-cycle-phase-related heterogeneity described above (Figure 2D), two clusters expressed genes linked to specific cell-cycle phases. Cells of c2 showed a high expression of genes active in the S phase, including *E2F1*, *TYMS*, and *RRM2*, while cells of c4 showed a high expression of genes active in G<sub>2</sub>/M, including *MKI67*, *TOP2A*, and *UBE2C* (Figure 3B). Cell-cycle-phase scoring of the cells and enrichment analysis of the DE genes confirmed the S- and G<sub>2</sub>/M-associated states (Figures S3A and S3E). In agreement with aggressive tumors having increased proliferative activity, c2 and c4 consist predominantly of cells from high-risk patients (Figures 3C and S3F). Close to c2 and c4 resides a small cluster (c7) with a particularly elevated *MYCN* expression (Figures 3A and S3G). Also here, the *MYCN* targets *NEUROD1*<sup>49</sup> and *EZH2*<sup>50</sup> were highly expressed. Intriguingly, c7 also displayed enrichment for the recently described aggressive *MYCN*-high transitional state<sup>21</sup> (Figure S3H).

Cells from c0 mainly reside in the G<sub>1</sub> phase and expressed genes associated with sympathetic nervous system differentiation (and with favorable outcome), including *NTRK1* (encoding TRKA),<sup>51,52</sup> *CD9*,<sup>53</sup> and *STMN4*<sup>22</sup> (Figures 3B and S3E). Similarly, c3 showed a relatively high expression of genes that have also been associated with differentiation or favorable neuroblastoma, such as *GRID2*,<sup>54</sup> *DGKB*,<sup>52</sup> and *SST*.<sup>55</sup> Enrichment analysis of the DE genes for both clusters compared with all other clusters further supports a differentiated state (Figure S3A). Overall, cells from low- to intermediate-risk patients and patients without *MYCN* amplification are enriched in these two clusters displaying relatively low expression of *MYCN* (Figures 3B, 3C, and S3I).

Further, different clusters pointing to technical variation were identified. For c1, increased expression of ribosome

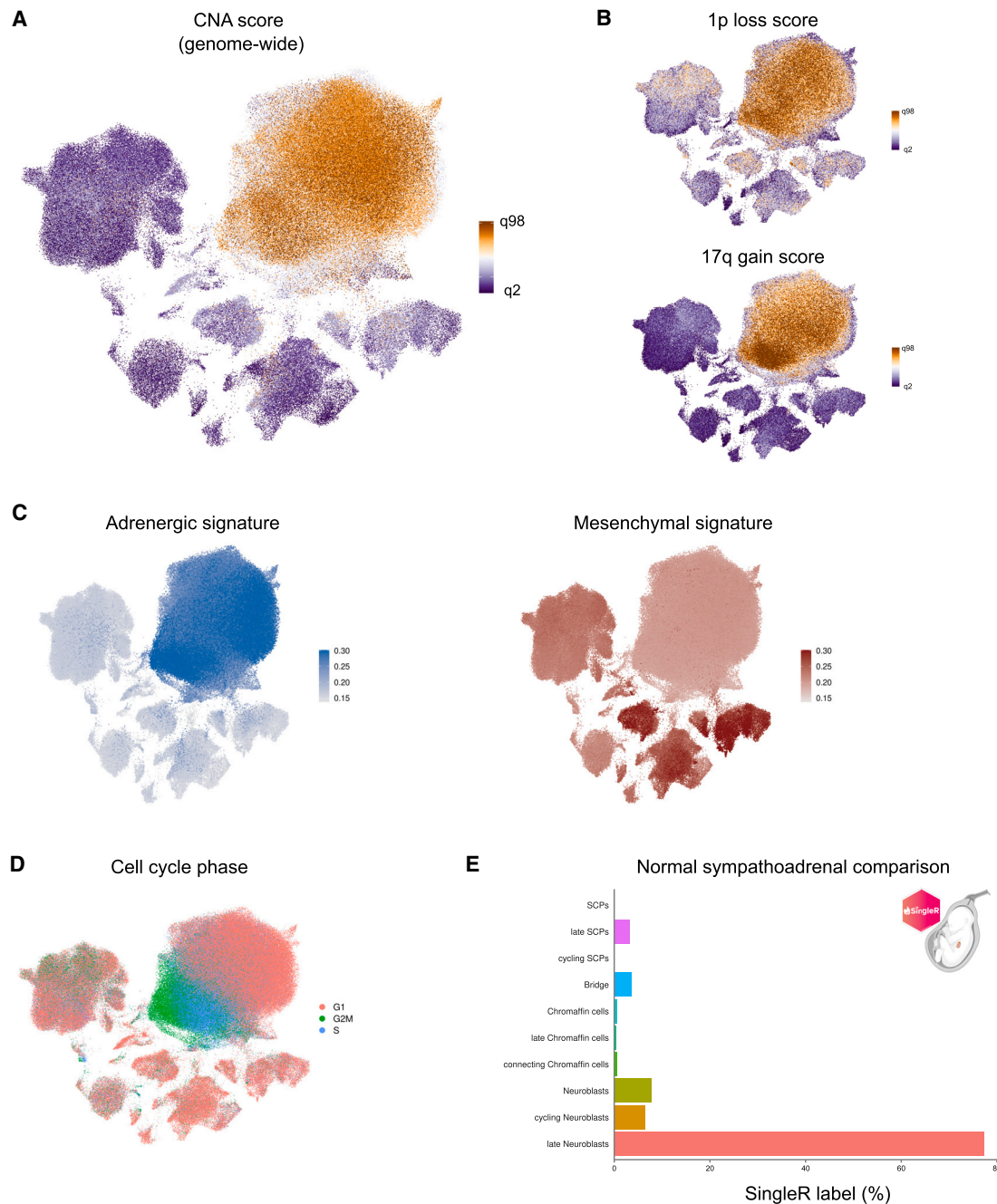


**Figure 2. Neuroendocrine cells present with molecular hallmarks of malignant neuroblastoma cells**

(A and B) Inferred copy-number alteration scores: (A) genome-wide, (B) 1p loss (top) and 17q gain (bottom). CNA, copy-number alteration; q2, second quantile; q98, 98<sup>th</sup> quantile.

(C) Adrenergic and mesenchymal signature scores (from van Groningen et al.<sup>39</sup>). Both signatures are set at the same scale to allow fair comparison of both signatures.

(D) Cell-cycle phase assignment of cells.

(E) Distribution of SingleR assigned labels after mapping neuroendocrine cells to normal sympathoadrenal development populations (from Jansky et al.<sup>16</sup>).

See also Figure S2.

biogenesis-associated genes (such as *NPM1*, *RPS15A*, and *RPS7*) was observed, which could suggest both elevated translation and technical artifacts in single-cell/nucleus data due to

sample-handling protocols<sup>56</sup> (Figures 3B and S3A). Likewise, a small cluster (c5) with elevated mitochondrial genes and a low number of counts/genes was identified, likely resulting from

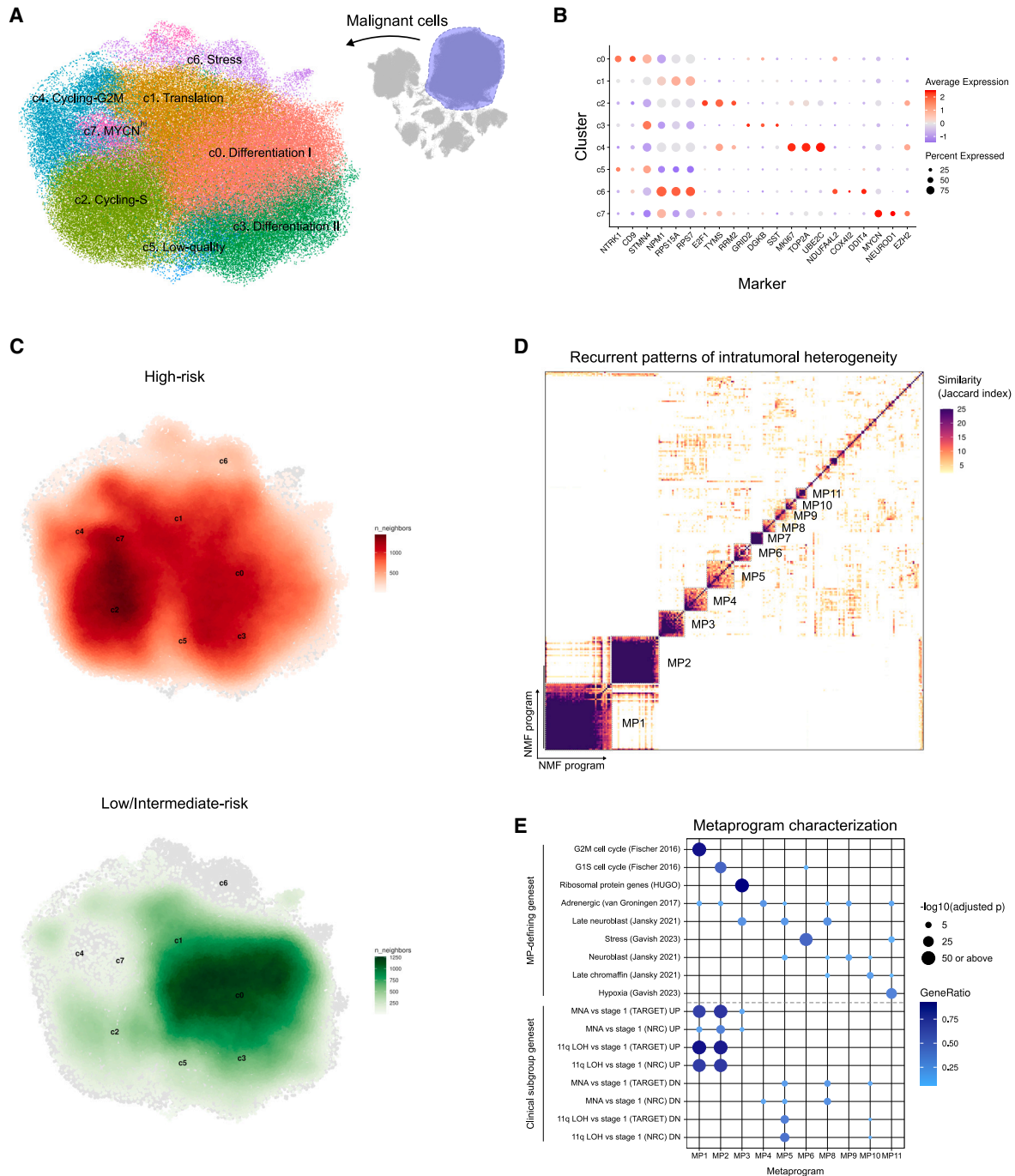


**Figure 3. Zooming in on malignant cell heterogeneity of neuroblastoma reveals distinct clusters linked to risk groups**

(A) Annotated UMAP of malignant tumor cells ( $n = 126,872$ ).

(B) Dotplot of top markers used for the annotation of (A).

(C) Density plot for cells from high-risk (top) vs. low-risk (bottom) patients.

(D) Heatmap of Jaccard similarity of robust NMF programs in tumor cells and clustering thereof into metaprograms.

(E) Functional enrichment of genes in the metaprograms. Metaprogram-defining gene sets (from Fischer et al.,<sup>46</sup> van Groningen et al.,<sup>39</sup> Jansky et al.,<sup>16</sup> and Gavish et al.<sup>47</sup>) and clinical subgroup-associated gene sets (from Rajbhandari et al.<sup>45</sup>) are shown. Only statistically significant results are shown. MP, metaprogram; UP, upregulated; DN, downregulated; MNA, MYCN amplified; LOH, loss of heterozygosity.

See also Figure S3.

technical variation (Table S3). Furthermore, c6 was enriched for stress-associated genes such as hypoxic markers *NDUFA4L2* and *COX4I2* and stress-induced *DDIT4* (Figure 3B). Accordingly, the expression of a signature for stress in tumor cells<sup>47</sup> is specifically high in this cluster (Figure S3J).

To scrutinize the tumor heterogeneity related to the adrenergic vs. mesenchymal cell identity, we investigated signatures<sup>39</sup> and established markers<sup>57</sup> for both identities. While some overlap of the DE genes of most tumor clusters with mesenchymal gene lists<sup>21,39,40</sup> can be found (Table S3), no tumor cluster expressed different key mesenchymal markers (Figure S3K). Moreover, only a limited number of tumor cells exhibited a van Groningen et al.<sup>39</sup> mesenchymal signature score using UCell<sup>58</sup> exceeding a background level (as determined using immune cells; Figures S3L and S3M). To further validate our findings, we used AUCell<sup>59</sup> with the same mesenchymal signature (by van Groningen et al.<sup>39</sup>) as well as with other mesenchymal signatures recently studied in human neuroblastoma tumors by Chapple et al.<sup>60</sup> This analysis consistently revealed that only a minute fraction of tumor cells (0%–0.07%) had an active mesenchymal expression program, while nearly all cells (99.86%) showed an active adrenergic expression program (Figure S3N). Consequently, we do not find conclusive evidence for an unequivocal cluster of mesenchymal tumor cells, and further validation of potential rare mesenchymal-like tumor cells is warranted (see discussion).

Further in line with this, upon comparison to normal sympathoadrenal populations, all clusters most closely resembled developing neuroblasts (Figure S3O). While for the DE genes of the cycling tumor cells (c2 and c4) there is a considerable overlap with those of both cycling neuroblasts and cycling Schwann cell precursors (SCPs),<sup>16</sup> only a resemblance to (cycling) neuroblasts can be noted. This suggests that this overlap with genes overexpressed in cycling SCPs may be attributed solely to their shared proliferative characteristics. In addition, among all clusters, cluster c7 displayed the highest proportion of cells resembling bridging cells (20.8%) and late SCPs (11.0%), further indicating a transitional state. Finally, next to the neuroblast-like identity, there are noticeable resemblances to other populations, particularly bridging cells and, to a lesser extent, connecting/late chromaffin cells and late SCPs (Figure S3O).

### Metaprograms independently validate the annotated tumor-cell clusters and associate with survival

To support the functional annotation of the identified tumor cells across different neuroblastomas, we included a different approach that does not rely on batch correction of the data from the different tumors. To this end, malignant gene-expression patterns were identified using non-negative matrix (NMF) factorization for each sample individually, as described by Gavish et al.<sup>47</sup> Application of this approach across different tumor samples led to the identification of NMF programs that clustered into 11 recurring gene-expression programs, termed metaprograms (MPs) (Figure 3D). These MPs were functionally characterized based on their top defining genes (Figure 3E and Table S4).

The two largest MPs were cell-cycle-phase related: G<sub>2</sub>/M and S phase for MPs 1 and 2, respectively (Figures 3D and 3E; Table S4). Interestingly, both programs were enriched in gene sets associated with clinical subgroups with poor outcome<sup>48</sup>

(Figure 3E and Table S4). Also, enrichment of FOXM1-target gene sets that are associated with aggressive neuroblastomas<sup>46,61,62</sup> was observed, most strongly for MP 1 (Table S4). Of note, MPs 1 and 2 contain several genes with therapeutic potential for neuroblastoma drugging, such as *RRM2*,<sup>63</sup> *AURKA*,<sup>64</sup> *TPX2*,<sup>65</sup> and *BIRC5*.<sup>52</sup> Additionally, several MPs showed enrichment for gene sets associated with clinically favorable subgroups,<sup>48</sup> including, MPs 4, 5, 8, and 10 (Figure 3E). These MPs typically showed enrichment of adrenergic genes.<sup>39</sup> Furthermore, different MPs (MPs 4, 5, 8, 9, and 10) were enriched for multiple cell types of sympathoadrenal development, including mainly neuroblast populations but also chromaffin, bridge cells and SCP populations (Table S4).

Finally, three MPs were more related to technical bias and stress. MP 3 contained almost exclusively ribosomal protein genes, indicative of technical artifacts,<sup>47</sup> and was thus not further investigated. Similarly, MPs 6 and 11 were stress- and hypoxia-related programs, respectively. MP 6 could further be attributed to experimentally induced (technical) stress, as this MP was also enriched for enzymatic-dissociation-associated signatures<sup>47,66</sup> and, consistent with this, was specifically observed in single-cell and not in single-nucleus data, where only single-cell data require enzymatic tissue dissociation (Table S4).

To relate the MP results with the previously identified tumor clusters, a signature for each MP was investigated in the integrated dataset (Figures S3P and S3Q). Overall, MP 4 was highly active across all transcriptional clusters, suggesting a pan-neuroblastoma program. As expected, the cell-cycle-driven and aggressive MPs 1 and 2 were most highly expressed in the G<sub>2</sub>/M and S clusters, respectively. Conversely, other MP signatures were more active in the low- to intermediate-risk and differentiation-associated clusters (i.e., MP 5 in both, MP 8 in c0, and MPs 9 and 10 in c3; Figures S3P and S3Q). Finally, the expression of the stress-associated MPs, 6 and 11, further corroborated the stress-related identity of c6.

Since the previous results suggest that some MPs are potentially linked to patient outcomes, we investigated the MP signatures in bulk RNA data of two large cohorts of neuroblastoma patients, i.e., the SEQC<sup>67</sup> (*n* = 498 patients) and NRC<sup>48</sup> (*n* = 276 patients) cohorts (Figure S3R). High expression of MPs 1, 2, and 3 was associated with decreased overall survival in both cohorts. A similar but less significant association was observed for MP 11. Oppositely, high expression of MPs 5, 8, 9, or 10 was associated with better overall survival in both cohorts.

Overall, assessment of gene-expression patterns in the tumor cells of different patients yields results highly similar to an integrated clustering of these cells. Together, these complementary analyses point to an association of distinct transcriptional profiles with patient outcomes, highlighting the clinical relevance of the observed transcriptional heterogeneity in neuroblastoma.

### Distinct populations of lymphoid and myeloid cells characterize the neuroblastoma tumor immune microenvironment

High-risk neuroblastomas are typically considered to be immunologically “cold” tumors,<sup>11</sup> which possess significant challenges for the development of possible immunotherapy

strategies. Nevertheless, in our NBT Atlas, we were able to detect and annotate several immune-cell types (Figure 1C), which we next examined in more detail. To this end, we isolated the immune-cell clusters (T cells, NK cells, B cells, plasma cells, pDCs, and myeloid cells) from the different patients and reclustered them using scVI to generate a uniform manifold approximation and projection (UMAP) consisting of 91,750 cells/nuclei (Figures 4A and S4A). The increased resolution allowed a more in-depth characterization of the initially broadly classified cells. Examination of the DE genes (Table S5) revealed the presence of numerous lymphoid populations, including CD4<sup>+</sup> T cells, regulatory T cells (Tregs), CD8<sup>+</sup> T cells, NK T cells, circulating NK cells, resident NK cells, a small population of *TOX2*- and *KIT*-expressing NK cells, B cells, and pDCs, each with their own unique gene-expression profiles (Figures 4A and 4B; Table S5). Notably, lymphoid cells were found to be the most abundant immune cells (80.1%; Figure S4B), a finding that is quite striking, especially given the proposed limited lymphocyte infiltration in neuroblastoma.<sup>11,68</sup> This raises the possibility of artifacts resulting from the tissue digestion required for single-cell RNA-seq analyses whereby circulating cells (largely lymphoid) are considerably easier to liberate as compared with tissue-resident cells (largely myeloid), potentially leading to an over-representation of lymphoid cells in the single-cell RNA-seq data (discussed further below).

Despite their low abundance, given the proposed importance of myeloid cells in neuroblastoma in terms of antigen presentation (e.g., dendritic cells [DCs]) and modulation of the TME (e.g., macrophages, neutrophils),<sup>18,20,70,71</sup> we further assessed the heterogeneity within these cells. Here, we identified cDC1s based on the expression of *XCR1*, *CLEC9A*, and *CADM1* (Figures 4A and 4B), three marker genes previously shown to identify these cells across tissues and species.<sup>72</sup> Likewise, a population of cDC2s was identified based on the expression of *CD1C*, *CD1E*, and *CLEC10A* (Figures 4A and 4B). Recently, a newly identified population of DCs, termed DC3s, has been described in inflamed and injured tissue, showing considerable transcriptomic overlap with cDC2s.<sup>73–77</sup> As accurately distinguishing between these populations was not possible, given the low number of cells ( $n = 1,988$ ), here, we have annotated these cells as cDC2/DC3 (Figures 4A and 4B). Further investigation is thus needed to explore heterogeneity within this population and its implications for T cell responses. In addition to cDC1s and cDC2s/DC3s, a third population of DCs, namely migratory cDCs, i.e., cDCs poised to migrate to the draining lymph nodes where they will induce naive T cell differentiation and expressing *CCR7*, *LAMP3*, and *CCL19*, was also identified (Figures 4A and 4B). In addition to the cDCs, a small population of neutrophils (*FCGR3B*<sup>+</sup>, *CMTM2*<sup>+</sup>, and *CXCR2*<sup>+</sup>) was also identified within the myeloid cells alongside a larger population of monocytes and macrophages expressing *CD14*, *MAFB*, *CSF1R*, and *CD68* (Figures 4A and 4B). Previously, so-called myeloid-derived suppressor cells (MDSCs) were also identified in neuroblastoma.<sup>18</sup> However, as MDSCs can include monocytes, neutrophils, and potentially also some macrophages, this has sparked debate over the usefulness of this term, especially in this era of single-cell analyses.<sup>78</sup> Based on this ongoing discussion, we have not annotated any cells as MDSCs. Never-

theless, as this term is widely used, including in previous neuroblastoma studies,<sup>18,71,79–81</sup> for comparative purposes we mapped the MDSC annotation (from Costa et al.<sup>18</sup>) onto our immune-cell UMAP, revealing these cells to be neutrophils (Figure S4C).

### Multiple subsets of macrophages with distinct activation profiles exist in neuroblastoma

Given their hypothesized importance in the neuroblastoma TME,<sup>70,71,82</sup> we next aimed to increase the resolution for the monocytes and macrophages identified in the immune-cell atlas. Reintegration and clustering analysis identified 11 subsets and/or activation states across different patients, including a cluster of proliferating cells (Figures 4C, 4D, and S4D; Table S6). First, classical (*VCAN*<sup>+</sup>, *S100A12*<sup>+</sup>, *THBS1*<sup>+</sup>, *EREG*<sup>+</sup>) and patrolling (or non-classical) monocytes (*SPN*<sup>+</sup>, *FCGR3A*<sup>+</sup>, *FCGR3B*<sup>+</sup>, *CX3CR1*<sup>+</sup>) could be distinguished from the macrophages (which were identified based on expression of generic markers including *C1QA*, *C1QB*, *C1QC*, *CSF1R*, *MAFB*, and *CD68*). Analysis of these genes also revealed the presence of a population of monocytes likely in the process of transitioning to macrophages (termed “*CLEC10A*<sup>+</sup> trans mono”) expressing lower levels of both macrophage and monocyte-defining genes alongside specific genes for this cluster such as *CLEC10A*, *IDO1*, and *LGALS2* (Figures 4C and 4D). This suggests that in neuroblastoma, monocytes are recruited to the tumor and/or TME and subsequently differentiate into macrophages. Among the macrophages, we identified seven non-proliferating clusters, of which one consisted of lower-quality cells with limited DE genes and enrichment for ribosomal genes (termed high ribosomal macs), which were not analyzed further (Figure 4C and Table S6). Among the remaining six clusters, we identified a population of macrophages expressing genes associated with lipid-associated macrophages (LAMs) previously described in the liver and adipose tissue,<sup>69,83,84</sup> including *TREM2*, *SPP1*, *FABP5*, *CD9*, and *GPNMB* (Figures 4C and 4D). Indeed, mapping our recently defined conserved human-mouse LAM signature<sup>69</sup> onto this dataset corroborated the assignment of this population as LAMs (Figure 4E). Alongside identifying the cluster of LAMs, the LAM signature expression also revealed two smaller populations of cells with an LAM-like phenotype expressing some but not all of the LAM-associated genes. Notably, these clusters also expressed some unique genes, with one cluster expressing *BEST1* and *ALDOA* (*BEST1*<sup>+</sup> LAM-like) and the other expressing *RBP4* and *GPD1* (*RBP4*<sup>+</sup> LAM-like). However, as both of these clusters were unique to one or two patients (Figure S4D), this makes it difficult to draw any conclusions about these cells, and we did not examine them further. Aside from the LAM and LAM-like macrophages we also identified two clusters expressing *FOLR2*, which could be further distinguished by their expression of *CD163* and *CETP*, respectively (Figures 4C and 4D). *FOLR2*<sup>+</sup>*CETP*<sup>+</sup> macrophages also expressed the highest levels of HLA genes. Lastly, this analysis also revealed the presence of a population of macrophages co-expressing *MMP9* and *PLA2G2D* (Figures 4C and 4D).

To gain some insight into the potential functional relevance of this macrophage heterogeneity, we next examined whether any of the subsets could be correlated with patient risk or

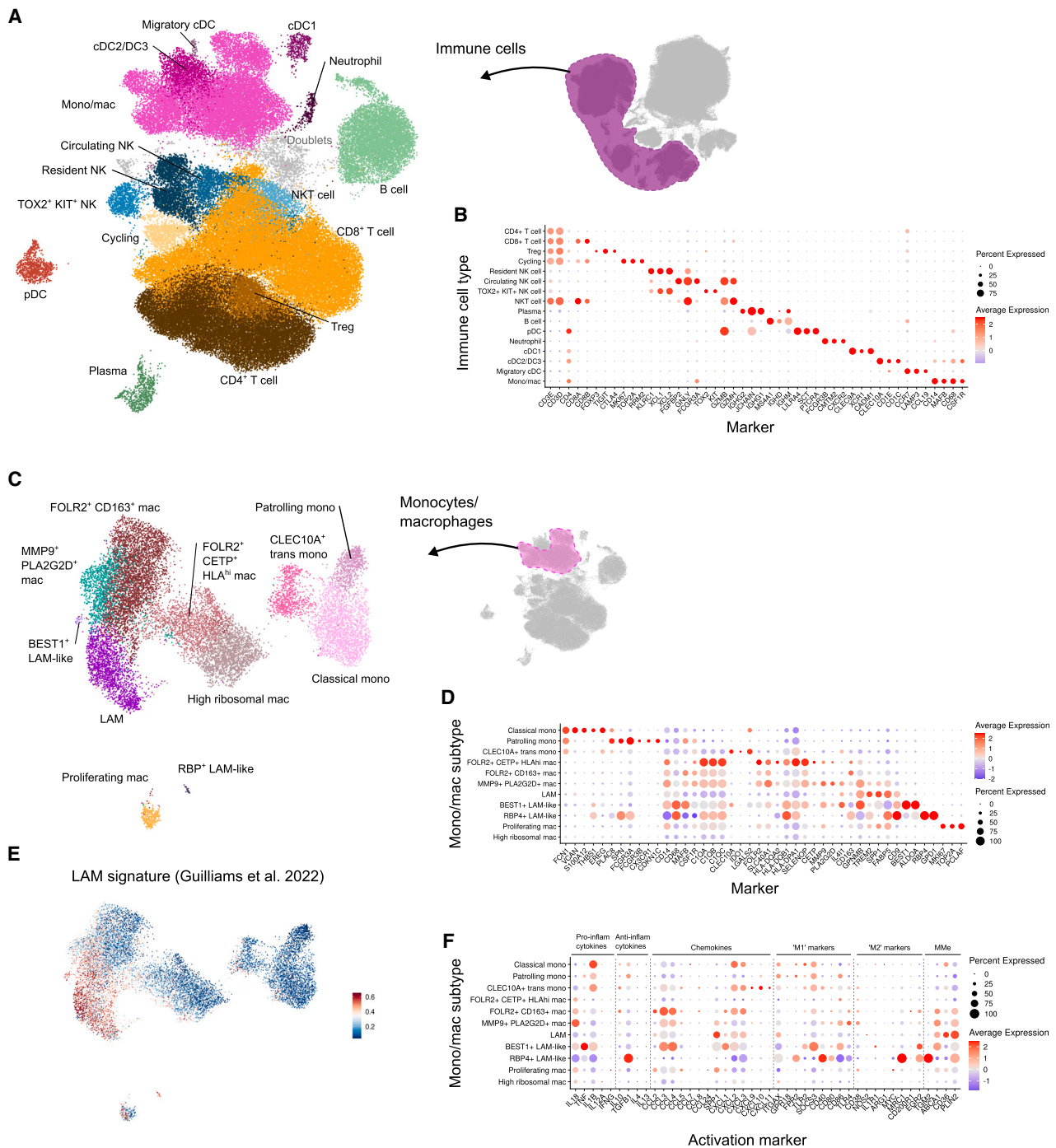


**Figure 4. Distinct populations of lymphoid and myeloid cells characterize the neuroblastoma tumor immune microenvironment**

(A) Annotated UMAP of immune cells ( $n = 91,750$  cells; doublets excluded).

(B) Dotplot of markers used for annotation in (A).

(C) Annotated UMAP of monocytes and macrophages ( $n = 14,860$ ).

(D) Dotplot of markers used for annotation in (C).

(E) LAM signature (from Guilliams et al.<sup>69</sup>) expression in monocytes and macrophages.

(F) Activation marker expression in monocytes and macrophages. mac, macrophage; mono, monocyte; LAM, lipid-associated macrophage; rel., relative; inflam, inflammatory; MMe, metabolically activated macrophages.

See also Figure S4.

treatment. Since 79% (or 11,669/14,860) of cells are from high-risk patients, a similar fraction is expected for each monocyte/macrophage population, which was the case for most populations (Figure S4E). However, LAMs, identified in 53 of the 67 patients profiled appeared to show a trend to be more prevalent in high-risk neuroblastoma samples (although not statistically significant here; Figure S4E). To further investigate the potential immunosuppressive role of LAMs, as described across different cancer types,<sup>85–88</sup> we next examined the expression of several genes associated with macrophage-activation states across the different macrophage populations<sup>83</sup> (Figure 4F). Contrary to what has previously been suggested using a limited number of patients,<sup>20</sup> this did not reveal a prototypical immunosuppressive phenotype (Figure 4F). Indeed, considering all macrophage populations, the expression of activation-associated genes did not align with clear pro-inflammatory or immunosuppressive/repair phenotypes in the distinct populations/stages, consistent with the idea that these macrophage-activation states (commonly referred to as M1 and M2, respectively) represent *in vitro* phenomena that are not replicated *in vivo*, likely as a result of the plethora of signals these cells receive simultaneously *in vivo* compared with *in vitro*.<sup>89</sup> We also could not find enrichment of previously published gene-expression modules associated with human *in vitro* M1 and M2 macrophage states<sup>90</sup> in the identified macrophage populations (Figure S4F), further highlighting the need to carefully consider the relevance of these M1/M2 signatures when analyzing macrophages *ex vivo*.

Taken together, this analysis demonstrates considerable heterogeneity within the macrophage compartment in neuroblastoma and highlights that further research is required to assess the functional relevance of this heterogeneity.

#### Technical differences between single-cell and single-nucleus RNA-seq-based transcriptomics

In addition to delineating distinct compartments within the NBAtlas, it is crucial to consider the data composition of the atlas itself, which is a collection of both single-cell and single-nucleus RNA-seq data. For different cell types, we noted a general agreement between the expression profiles generated using both approaches (Figure S5A), consistent with previous studies.<sup>91,92</sup> While each technique has its advantages, single-cell- and single-nucleus-specific genes are also observed, so here we sought to better understand how the assay influences the data generated. First, we noted an elevation of tissue-dissociation-associated stress signatures<sup>66</sup> in single-cell data (Figure S5B). Consistent with this, the stress-associated tumor cluster (c6) and MP 6 we described above were enriched specifically in single-cell samples. Moreover, we found that the fraction of neuroendocrine cells recovered in single-cell RNA-seq experiments was smaller than that recovered from single-nucleus RNA-seq (Figure 5A,  $p < 0.0001$ , one-sided Wilcoxon rank-sum test). To confirm this technical discrepancy independent of the atlas, we performed both single-cell and single-nucleus RNA-seq on tissue pieces from the same neuroblastoma tumor (Figure 5B and Table S1). Consistent with the NBAtlas, this revealed that a large population of neuroendocrine cells was captured with single-nucleus RNA-seq, while this population was almost ab-

sent in the corresponding single-cell RNA-seq data (Figure 5C; 46.4% vs. 0.2%, or 26,928/58,083 vs. 119/63,703).

Apart from the relative tumor fraction, we also noticed a difference in the immune-cell composition captured with single-cell vs. single-nucleus RNA-seq (Figures 5D, S5C, and S5D). Compared with single-nucleus RNA-seq, single-cell RNA-seq data were enriched for cells primarily found in circulation, including T cells, NK cells, and neutrophils. In contrast, single-nucleus datasets were enriched for what are typically considered tissue-resident cells, including cDCs and macrophages/monocytes. This suggests that tissue dissociation associated with single-cell RNA-seq protocols may preferentially isolate circulating cells over tissue-resident cells, leading to a bias in cell proportions as in previously described other tissues.<sup>19,29,69,91,93</sup> Since the NBAtlas data are primarily composed of samples analyzed by single-cell RNA-seq, this likely explains the unexpected majority of lymphoid vs. myeloid cells described above. We also investigated this in our in-house case for which we have matching single-cell and single-nucleus samples, as well as for a published matching single-cell and single-nucleus case,<sup>19</sup> which corroborated the trend toward lymphoid cell enrichment and myeloid cell absence in single-cell vs. single-nucleus datasets (Figures S5E and S5F).

#### The NBAtlas allows reference-based mapping of additional single-cell/single-nucleus data

An important challenge in single-cell/single-nucleus analyses remains cell-type annotation, requiring expert knowledge for manual annotation or a robust reference atlas for data-driven annotation. Therefore, we lastly evaluated the performance of the NBAtlas as a reference for cell annotation of future neuroblastoma single-cell or single-nucleus RNA-seq data. To this end, we generated additional single-cell and single-nucleus data for three and five neuroblastoma tumor samples, respectively (across six different patients, Table S1). As expected from the NBAtlas dataset, these samples displayed obvious batch effects (as discussed above, Figure S6A). This additional dataset was then used as a query for reference-based mapping with the NBAtlas (Figure 6A). We took advantage of guided integration using scArches<sup>30</sup> to simultaneously integrate our in-house data and expand the NBAtlas, which is not possible with conventional mapping methods such as SingleR. Following this data processing, the cell-type segregation and dataset harmonization of the NBAtlas were maintained (Figures S6B and S6C).

Since integration was performed using the scANVI-scArches pipeline, a cell-type prediction of the additional data was also provided. To set a baseline for comparison of cell-type prediction, cells from the additional dataset were also annotated manually before integration (Figure 6B). When comparing with the scANVI-scArches cell-type prediction based on the NBAtlas as a reference atlas, agreement with manual annotation reached 92.6% (or 50,559/54,574 and 4/54,574 undefined; Figure 6C). However, Schwann cells (*CDH19*<sup>+</sup>) and plasma cells (*IGHG1*<sup>+</sup>) were incorrectly annotated as fibroblasts and B cells, respectively (Figures 6C and S6D). Of note however, both cell types closely resemble their erroneously predicted counterpart and are also both present at low numbers in the reference atlas

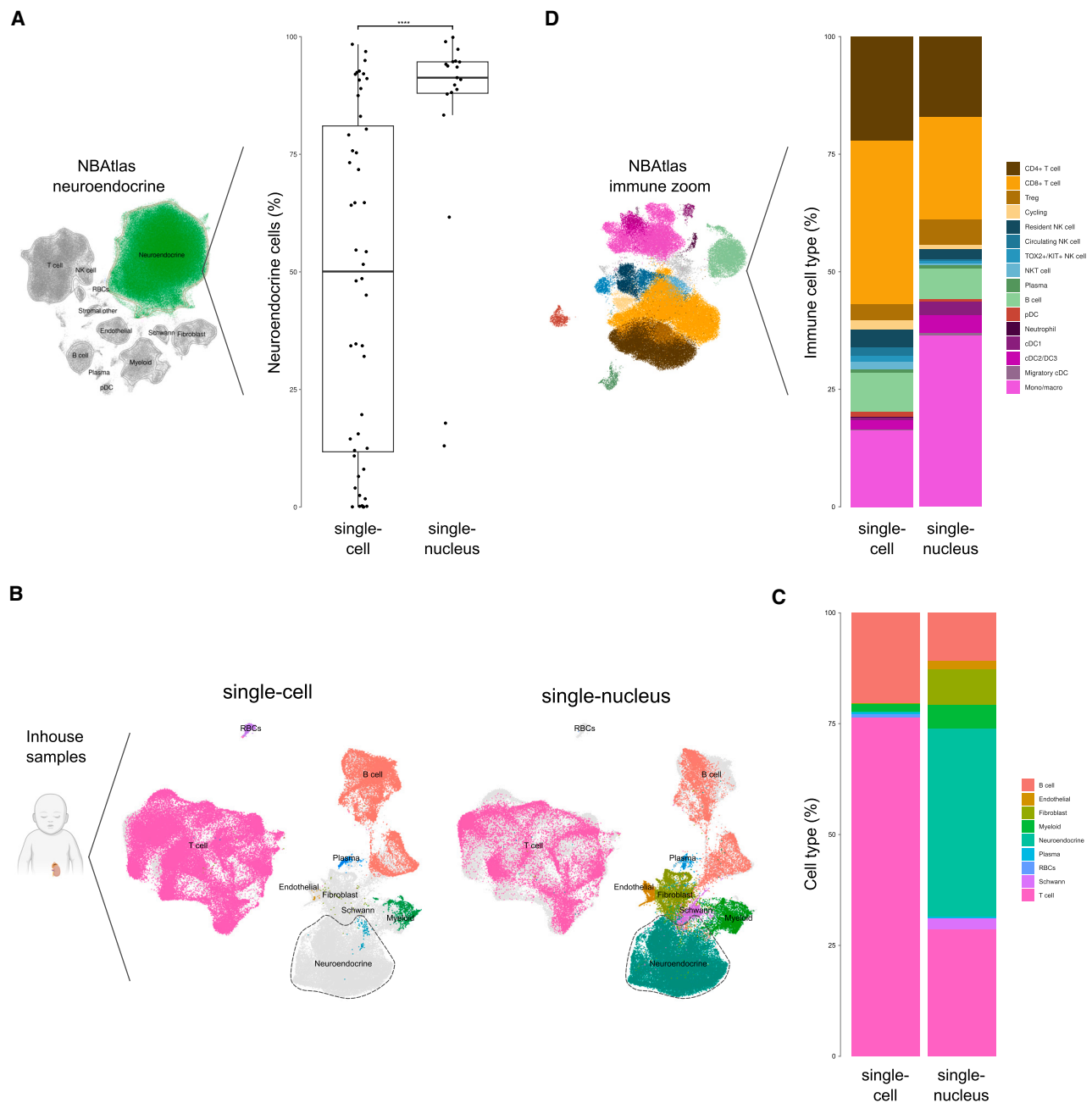


**Figure 5. Technical differences between single-cell and single-nucleus RNA-seq-based transcriptomics**

(A) Comparison of the fraction of neuroendocrine cells for single-cell ( $n = 48$ ) vs. single-nucleus ( $n = 19$ ) RNA-seq samples in the NBAtlas. Statistical significance was assessed with a one-sided Wilcoxon rank-sum test. \*\*\*\* $p < 0.0001$ .

(B) UMAPs highlighting cells derived from single-cell (left,  $n = 58,083$  cells) and single-nucleus (right,  $n = 63,703$  nuclei) RNA-seq of matching in-house samples from one neuroblastoma patient tumor.

(C) Cell-type proportions of (B).

(D) Comparison of the NBAtlas immune-cell-type proportions for single-cell vs. single-nucleus data ( $n = 88,743$  and  $n = 3,007$ , respectively). RBCs, red blood cells; mac, macrophage; mono, monocyte.

See also [Figure S5](#).

(0.2% or 655/362,991 for plasma cells, and 0.5% or 2,060/362,991 for Schwann cells) and thus cannot be considered as substantial errors.

In addition, we tested cell-type prediction using SingleR, which overall displayed less agreement with our manual annotation when with scANVI-scArches, reaching 78.0%

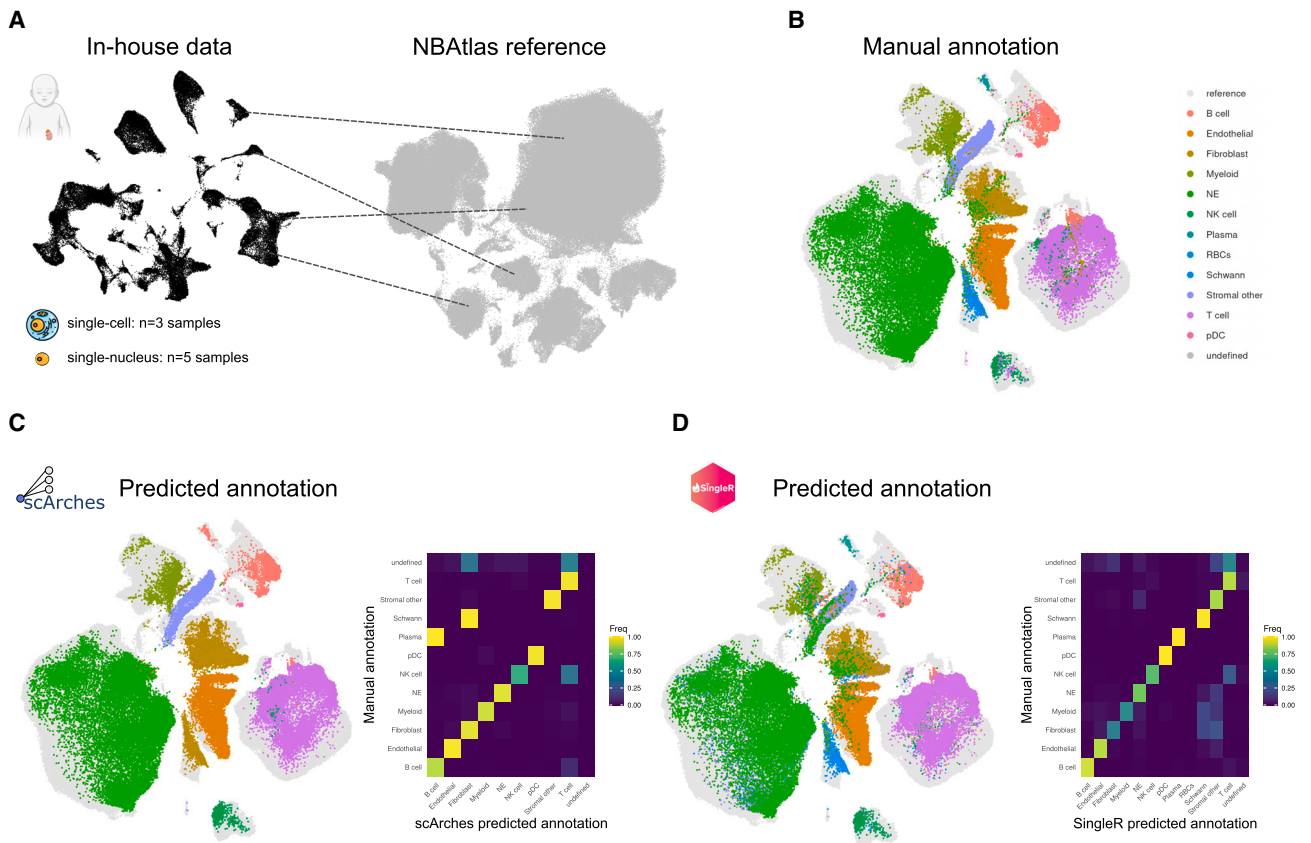


**Figure 6. The NBAtlas allows reference-based mapping of additional single-cell/nucleus data**

(A) Schematic representation of reference-based mapping of in-house-generated data ( $n = 3$  single-cell samples,  $n = 17,096$  cells and  $n = 5$  single-nucleus samples,  $n = 50,080$  nuclei).

(B) Manual annotation of in-house data (performed per sample) plotted on the scArches output integrated UMAP.

(C) scANVI-scArches cell-type prediction of in-house data plotted on the scArches integrated UMAP (left) and compared to manual annotation (right). Freq, relative frequency.

(D) SingleR cell-type prediction of in-house data plotted on the scArches integrated UMAP (left) and compared to manual annotation (right). Freq, relative frequency.

See also Figure S6.

(42,591/54,574 and 1.2% or 661/54,574 undefined) (Figure 6D). Of note, contrary to the scANVI-scArches prediction, SingleR was able to differentiate between plasma and B cells as well as Schwann cells and fibroblasts. However, many cells were erroneously assigned to “stromal other” (i.e., adrenal cortex). Indeed, different stromal cell types (including endothelial, fibroblast, Schwann, or “stromal other” cells) show similarity to one another, so these errors can be attributed to commonly shared markers between these populations (Figure S6E).

In summary, we illustrated the suitability of using the NBAtlas as a reference for integration and cell-type annotation of additional neuroblastoma single-cell transcriptome datasets.

## DISCUSSION

This study presents a harmonized comprehensive transcriptomic atlas of neuroblastoma tumors at single-cell resolution. The NBAtlas integrates seven different datasets, including both

single-cell and single-nucleus RNA-seq data, spanning over 360,000 cells from 68 different samples. We demonstrate that our atlas is harmonized over the different technical factors while preserving biological heterogeneity within both the tumoral and the immune-cell compartments and show that it is a useful tool to integrate and annotate neuroblastoma single-cell/nucleus datasets. Our NBAtlas enables the exploration of the intratumoral heterogeneity at the transcriptional level in a large collection of neuroblastoma tumors and supports investigating hypotheses regarding pathobiology. To facilitate further exploration of our atlas, we have made the NBAtlas interactively available on <https://single-cell.be/nbatlas> and on the R2: Genomics Analysis and Visualization platform ([https://hgserver2.amc.nl/cgi-bin/r2/main.cgi?dscope=NBSCA&option=about\\_dscope](https://hgserver2.amc.nl/cgi-bin/r2/main.cgi?dscope=NBSCA&option=about_dscope)), and it is also available for download (see deposited data in the [key resources table](#) in STAR Methods).

Our NBAtlas is focused on transcriptomic data for tumor samples from neuroblastoma patients. Future studies could expand

the current atlas to also include single-cell data from cell lines, xenograft models, allograft models, and developmental models relevant to neuroblastoma. Also, recently a single-cell ATAC-seq dataset has been published for neuroblastoma bone-marrow metastases.<sup>94</sup> By adding other modalities such as chromatin accessibility or DNA methylation, an even more complete picture of the tumoral heterogeneity will be acquired, ultimately improving our understanding of the complex disease that is neuroblastoma.

In the current NBAtlas, a notable observation was the presence of significant tumoral heterogeneity at the cell-cycle level, consistent with many molecular mechanisms related to cell-cycle-driving neuroblastoma. A prime example of this is the replication-stress pathway to which neuroblastoma cells are addicted.<sup>63</sup> We found high activity of signatures related to this pathway in cycling neuroblastoma cells which were almost absent in TME cells. This included a signature for sensitivity to prexasertib, an effective drug *in vitro* and *in vivo* in combination with triapine for targeting the replication-stress pathway in neuroblastoma.<sup>63</sup> As a public resource (see deposited data in the [key resources table](#) in *STAR Methods*), further signatures including those predicting additional drug sensitivities can now also be explored at a single-cell level.

The two proposed cell states for neuroblastoma tumor cells are the adrenergic (or noradrenergic)-like and the mesenchymal (or neural crest)-like fates, with the latter being linked to chemoresistance.<sup>39,40</sup> While the presence of adrenergic-like tumor cells is well established, the observation of mesenchymal-like cells in human tumor samples remains a topic of debate. Most studies identifying mesenchymal cells typically rely on *in vitro* cell lines<sup>23,39</sup> or bulk transcriptomic/epigenetic sequencing methods in patients,<sup>41</sup> which fail to discriminate between mesenchymal-like tumor cells and stromal cells. Most single-cell studies do not identify malignant mesenchymal cells.<sup>15–18,22</sup> However, there are a few single-cell studies hinting at the presence of these cells: (1) using Smart-seq2, a malignant mesenchymal cluster was proposed but only in post-treatment neuroblastoma, which limits generalizability<sup>21</sup>; (2) a separate study for samples at diagnosis and relapse proposed a population of “noradrenergic with mesenchymal features”<sup>23</sup>; and (3) a study by Chapple et al.<sup>60</sup> identified a rare weak mesenchymal-like expression program in otherwise adrenergic tumor cells (“Mes-weak”) that transitioned into mesenchymal cells under chemotherapy in a murine neuroblastoma model (“Mes-EMT-like”). In the NBAtlas, we identified mesenchymal signatures primarily in Schwann cells and fibroblasts, which did not present with CNAs. Among the tumor cells, we only found a few cells with a notable mesenchymal signature expression; however, these cells did not form a separate cluster. Consequently, further research will be necessary to provide convincing evidence for a bona fide mesenchymal subpopulation, as these cells could also be attributed to the technical limitations of the CNV inference algorithm due to the noisiness of the input data. Nonetheless, we cannot rule out the existence of malignant mesenchymal cells in minute fractions, possibly due to their transient nature and selection pressure toward adrenergic fate *in vivo*, especially during chemotherapy.<sup>23,42,60</sup> Nevertheless, as demonstrated in other tumor entities,<sup>95</sup> unambiguous detection of mesenchymal-like tumor

cells requires evidence beyond single-cell RNA-seq data alone, such as spatial omics.

Next to adrenergic-mesenchymal heterogeneity, we also investigated additional transcriptional heterogeneity within the neuroblastoma tumor cells. To this end, we performed and annotated an unsupervised cell clustering of the tumor-cell populations identified in the integrated dataset. To orthogonally and independently validate these integration results, we identified intratumoral heterogeneity programs (“MPs”) in individual tumors without integration. A number of these programs were found to be reoccurring across different patients and were highly similar to the integrated tumor clusters, demonstrating that biological heterogeneity was preserved during integration. Cell states with high expression of genes involved in cell-cycle progression were primarily identified in cells from high-risk patients and were linked to poor overall survival. We also identified cells mostly originating from low- to intermediate-risk patients expressing more differentiation-related markers and signatures linked to a better outcome. In addition, we identified ribosomal protein gene enrichment in some tumor-cell clusters (c1 and c6) and one MP (MP3) which could indicate either a technical artifact of sample handling or a biological signal related to ribosome biogenesis that was correlated to poor survival, consistent with previous reports.<sup>96</sup> A more in-depth understanding of the functions of these diverse neuroblastic cell states therefore warrants further investigation.

Further, by compiling the tumor cells of over 50 patients included in the NBAtlas, a comprehensive comparison was possible with cells during normal development<sup>16</sup> as well as with an *in vitro* model simulating sympathoadrenal development.<sup>45</sup> The transcriptome profile of most patient cells aligns with that of normal neuroblasts (also termed sympathoblasts), which is generally agreed to be the cell of origin of neuroblastoma.<sup>16,17,97</sup> Of note, features of other sympathoadrenal development populations such as bridge cells, chromaffin cells, and SCPs were also present in the tumor cells (as DE genes or in the NMF programs), reminiscent of the complex features of sympathoadrenal development. Therefore, more in-depth investigations are needed to pinpoint the exact events along the sympathoadrenergic differentiation track that leads to neuroblastoma development.<sup>98</sup>

Aside from examining the tumor cells, the integrated NBAtlas also allowed us to characterize the immune cells present within the TME across the different neuroblastoma samples. Over the past decade, it has become clear that a better understanding of the TME is key for the development of new (immuno)therapies.<sup>99,100</sup> Our analysis revealed the presence of multiple lymphoid and myeloid subsets, suggesting that it may indeed be possible to develop novel immunotherapy approaches targeting these cells. For example, the presence of cDC1s, cDC2/DC3s, and migratory cDCs, i.e., cDCs expressing *CCR7* and hence primed to migrate toward the tumor-draining lymph nodes where they can present any acquired tumor antigens to naive T cells to induce appropriate T cell responses, suggests that targeting these cells as proposed in other cancers<sup>101–104</sup> may be a viable therapeutic option. Moving forward, it is important to determine (1) where these cells are in the context of the tumor and surrounding tissue to assess their ability to acquire tumor

antigens, and (2) their ability to prime naive T cells. Similarly, the identification of a neutrophil population that had previously been associated with a suppressive phenotype<sup>18</sup> suggests that these cells may also be a potential therapeutic target. Of course, additional functional studies are required in this regard to formally demonstrate their immunosuppressive roles.

Another interesting finding from the immune landscape investigation in the NBAtlas was the considerable heterogeneity among tumor-associated macrophages (TAMs). Excluding monocytes and proliferating cells, we identified seven different subsets of TAMs in this study. One of the larger populations identified was a cluster we termed LAMs given their expression of *TREM2*, *CD9*, *GPNMB*, *SPP1*, and *FABP5*, and, hence, their overlap with LAMs previously identified across multiple tissues and species.<sup>69,83,84,105</sup> Notably, macrophages with a similar signature have also been described in the injured brain, injured heart, infected lung, and in the context of cancer,<sup>86,88,106–111</sup> suggesting that this signature may be one generally associated with injury, inflammation, and/or repair. Notably, while we called these cells LAMs based on their initial description in obese adipose tissue, the best annotation is currently being discussed, with a number of other names also being proposed, including FAB5 macrophages and scar-associated macrophages.<sup>105,112</sup> In the context of neuroblastoma, it will therefore also be informative to assess lipid load and location of these cells within the TME. Moreover, although *TREM2*-expressing macrophages and LAMs have been receiving considerable attention lately, their exact roles remain uncertain, with conflicting reports on their potential immunosuppressive<sup>86,88,113</sup> or beneficial functions.<sup>69,83,84</sup> Here, we noted a slight tendency for LAMs to be more prevalent in high-risk neuroblastoma, potentially fitting with an immunosuppressive role for these cells; however, such a putative function was not corroborated when activation states of these cells were assessed. In fact, there was no distinct immunosuppressive or pro-inflammatory phenotype associated with any of the macrophage populations identified, demonstrating the necessity for in-depth functional studies to elucidate the roles of the distinct macrophage populations.

Intriguingly and unexpectedly, lymphoid cells considerably outnumber myeloid cells in the NBAtlas, a finding inconsistent with previous immunohistochemical analysis of neuroblastoma samples.<sup>68</sup> However, by integrating single-cell and single-nucleus RNA-seq data in the NBAtlas and following the generation of matched data using both techniques, we were able to demonstrate that this enrichment is specifically observed for the single-cell RNA-seq samples, suggesting that this is an artifact of the tissue digestion protocols required to generate single-cell suspensions needed for single-cell but not for single-nucleus RNA-seq. Importantly, we also report a lack of neuroendocrine cells in single-cell vs. single-nucleus samples. Indeed, this is not the first time that single-cell RNA-seq analysis has been shown to report altered cell proportions compared with what is observed *in vivo* as assessed by imaging or by single-nucleus RNA-seq.<sup>19,29,69</sup> Furthermore, we specifically found increased tissue-dissociation-stress-associated gene expression in single-cell datasets as compared with single-nucleus datasets, likely due to the use of enzymes to generate single-cell suspensions, consistent with previous studies.<sup>66,69,91,114</sup> However, sin-

gle-cell RNA-seq also has benefits compared to single-nucleus RNA-seq due to profiling the transcriptome of the entire cell and not only the nucleus, including an increased number of profiled genes, which allows improved cell (sub)typing. Taken together, these technical considerations highlight the importance of combining methods when analyzing samples to avoid biased conclusions.

The NBAtlas represents a reference atlas for expansion with additional single-cell or single-nucleus datasets and cell-type annotation thereof. As a proof of principle, we integrated in-house-generated single-cell and single-nucleus neuroblastoma tumor data into the NBAtlas. We showed that a transfer-learning approach allows the expansion of the current atlas, which in the future might aid in the identification of rare new subpopulations that remain undetected. Furthermore, we also tested cell-type prediction using the NBAtlas as a reference in a data-driven way, avoiding manual annotation that is challenging and less reproducible. The scANVI-scArches pipeline showed excellent agreement overall with manual annotation. However, the pipeline was not able to distinguish some less common cell types from closely related cell types. The same cell-type prediction with SingleR showed overall less agreement with manual annotation compared to scANVI-scArches; however, the algorithm was able to distinguish between all cell types. We thus advise considering both reference-based cell-type annotation methods and cross-checking annotation where both predictions disagree by using the key markers we described in this study.

In conclusion, we formed a large, harmonized cell atlas of published neuroblastoma single-cell and single-nucleus RNA-seq data. The collective dataset has allowed us to identify adrenergic neuroendocrine cells as the tumor population, and we did not confidently detect a mesenchymal tumor-cell population. Transcriptome profiles within distinct subsets of tumor cells did link to patient outcomes, thus aiding in identifying the factors contributing to the low survival rates observed in high-risk patients. In addition, our in-depth immune-cell characterization identified a *TREM2*-macrophage population linked to high-risk disease, which offers potential avenues for therapeutic intervention. Furthermore, we revealed important differences in single-cell vs. single-nucleus RNA-seq data, which were largely unexplored in the context of neuroblastoma. Finally, our NBAtlas is a valuable resource for neuroblastoma tumor heterogeneity and will additionally facilitate the integration and analysis of future single-cell studies.

### Limitations of the study

We acknowledge limitations of the current study. Only 10x Genomics datasets were included in this study. Adding plate-based datasets (such as Smart-seq2) is unlikely to result in a significant increase in the number of total cells due to limited throughput and will make the integration task even more complex. However, since the sequencing depth is usually much higher for these data, these could add low-abundance transcripts, which could help further delineate cell populations. We focused on intratumoral heterogeneity and acknowledge that more subtle patient-specific expression patterns can get lost due to the applied integration for batch correction. Due to the different technical variables of the used datasets, between-patient comparisons

are more challenging with our atlas. Further, cell-type fraction differences between patients (or patient groups) in our atlas are limited in interpretability due to the influence of the technical differences between single-cell and single-nucleus samples. Finally, in terms of our analysis of the immune compartment in neuroblastoma, this study is limited in that here we have only described the subsets identified. The precise functional relevance of the different populations remains to be determined, as does the specific locations of these cells in the tumor and TME. While several challenges lie ahead, we took an important step forward in understanding the heterogeneity of neuroblastoma tumors across multiple patients with the development of this comprehensive atlas.

### RESOURCE AVAILABILITY

#### Lead contact

Further information should be requested from the lead contact, Katleen De Preter ([katleen.depreter@ugent.be](mailto:katleen.depreter@ugent.be)).

#### Materials availability

No unique reagents were generated.

#### Data and code availability

- Raw data of in-house generated single-cell and single-nucleus RNA sequencing is deposited in the European Genome-phenome Archive (EGA: EGAD50000000328).
- Processed count data of in-house generated single-cell and single-nucleus RNA sequencing is deposited in Gene Expression Omnibus (GEO: GSE253865).
- A Seurat object of the NBAtlas can be found here: Mendeley Data: <https://doi.org/10.17632/yhcf6787yp.1>.
- Our data can be visualized using <https://single-cell.be/nbatlas> and is available in the R2 genomics tool: [https://hgserver2.amc.nl/cgi-bin/r2/main.cgi?dscope=NBSCA&option=about\\_dscope](https://hgserver2.amc.nl/cgi-bin/r2/main.cgi?dscope=NBSCA&option=about_dscope).
- No novel code was generated for this study. The main code can be found at: [https://github.com/VIBTOBILab/NBAtlas\\_manuscript](https://github.com/VIBTOBILab/NBAtlas_manuscript) (Zenodo: <https://zenodo.org/records/13741873>).
- Any additional information required to reanalyze the data reported in this paper is available from the [lead contact](#) upon request.

### ACKNOWLEDGMENTS

We acknowledge the use and support of the following core facilities: VIB Single-cell Core, VIB Flow Cytometry Core, and VIB Sequencing Core. We also thank the HPC-UGent team for their support. We thank the authors of the used datasets for making their data publicly accessible. We thank Selina Jansky and Cécile Thirant for sharing their data. We are grateful for the discussions with Shenglin Mei. We also thank Cristina Pintucci for her help in acquiring data and administrative support. We thank Kevin Verstaen for his help in generating a visualization tool. We thank all patients and their families who participated. Some figures were created with [Biorender.com](https://biorender.com). This project was supported by Kom op tegen Kanker (STI.VLK.2017.0010.01 to K.D.P.), Stichting Tegen Kanker (F/2020/1455 to K.D.P. and V.V.) and Ghent University (BOF22/GOA/009 to F.S., C.L.S., and B.D.W.).

### AUTHOR CONTRIBUTIONS

Conceptualization, N.B., K.D.P., C.E., C.L.S., and V.V.; experiments, N.B., C.L.S., B.V., C.Z., and S.R.; data analysis, N.B., T.T., V.Z., and S.-L.B.; data curation, N.B., C.L.S., and A.V.H.; visualization, N.B.; software, J.K.; writing – original draft, N.B., K.D.P., C.L.S., and A.V.H.; writing – review & editing, N.B., K.D.P., A.V.H., C.L.S., F.S., C.E., J.K., V.Z., S.-L.B., and V.V.; funding acquisition, K.D.P., F.S., C.L.S., and V.V.; resources, B.D.W., C.L.S., N.V.R., L.M.M.,

S.V.H., S.S.R., C.T., and I.J.-L.; supervision, K.D.P., C.L.S., F.S., C.E., A.V.H., and V.V.

### DECLARATION OF INTERESTS

The authors declare no competing interests.

### DECLARATION OF GENERATIVE AI AND AI-ASSISTED TECHNOLOGIES IN THE WRITING PROCESS

During the preparation of this work, the authors used ChatGPT in order to improve readability and language. After using this tool/service, the authors reviewed and edited the content as needed and take full responsibility for the content of the publication.

### STAR★METHODS

Detailed methods are provided in the online version of this paper and include the following:

- KEY RESOURCES TABLE
- EXPERIMENTAL MODEL AND SUBJECT PARTICIPANT DETAILS
- METHOD DETAILS
  - Processing of published data into the NBAtlas
  - Tumor and immune zoom
  - In-house generated single-cell and single-nucleus RNA-seq data
  - Visualization
- QUANTIFICATION AND STATISTICAL ANALYSIS

### SUPPLEMENTAL INFORMATION

Supplemental information can be found online at <https://doi.org/10.1016/j.celrep.2024.114804>.

Received: February 1, 2024

Revised: June 11, 2024

Accepted: September 12, 2024

Published: October 3, 2024

### REFERENCES

1. Matthay, K.K., Maris, J.M., Schleiermacher, G., Nakagawara, A., Mackall, C.L., Diller, L., and Weiss, W.A. (2016). Neuroblastoma. *Nat. Rev. Dis. Primers* 2, 16078. <https://doi.org/10.1038/nrdp.2016.78>.
2. Körber, V., Stainczyk, S.A., Kurilov, R., Henrich, K.-O., Hero, B., Brors, B., Westermann, F., and Höfer, T. (2023). Neuroblastoma arises in early fetal development and its evolutionary duration predicts outcome. *Nat. Genet.* 55, 619–630. <https://doi.org/10.1038/s41588-023-01332-y>.
3. Ackermann, S., Cartolano, M., Hero, B., Welte, A., Kahlert, Y., Roderwieser, A., Bartenhagen, C., Walter, E., Gecht, J., Kerschke, L., et al. (2018). A mechanistic classification of clinical phenotypes in neuroblastoma. *Science* 362, 1165–1170. <https://doi.org/10.1126/science.aat6768>.
4. Hartlieb, S.A., Sieverling, L., Nadler-Holly, M., Ziehm, M., Toprak, U.H., Herrmann, C., Ishaque, N., Okonechnikov, K., Gartlgruber, M., Park, Y.-G., et al. (2021). Alternative lengthening of telomeres in childhood neuroblastoma from genome to proteome. *Nat. Commun.* 12, 1269. <https://doi.org/10.1038/s41467-021-21247-8>.
5. Mossé, Y.P., Laudenslager, M., Longo, L., Cole, K.A., Wood, A., Attiyeh, E.F., Laquaglia, M.J., Sennett, R., Lynch, J.E., Perri, P., et al. (2008). Identification of ALK as a major familial neuroblastoma predisposition gene. *Nature* 455, 930–935. <https://doi.org/10.1038/nature07261>.
6. Gröbner, S.N., Worst, B.C., Weischenfeldt, J., Buchhalter, I., Kleinheinz, K., Rudneva, V.A., Johann, P.D., Balasubramanian, G.P., Segura-Wang, M., Brabetz, S., et al. (2018). The landscape of genomic alterations

- across childhood cancers. *Nature* 555, 321–327. <https://doi.org/10.1038/nature25480>.
7. Rosswog, C., Fassunke, J., Ernst, A., Schömig-Markiefka, B., Merkelbach-Bruse, S., Bartenhagen, C., Cartolano, M., Ackermann, S., Theissen, J., Blattner-Johnson, M., et al. (2023). Genomic ALK alterations in primary and relapsed neuroblastoma. *Br. J. Cancer* 128, 1559–1571. <https://doi.org/10.1038/s41416-023-02208-y>.
  8. Schleiermacher, G., Javanmardi, N., Bernard, V., Leroy, Q., Cappo, J., Rio Frio, T., Pierron, G., Lapouble, E., Combaret, V., Speleman, F., et al. (2014). Emergence of new ALK mutations at relapse of neuroblastoma. *J. Clin. Oncol.* 32, 2727–2734. <https://doi.org/10.1200/JCO.2013.54.0674>.
  9. Eleveld, T.F., Oldridge, D.A., Bernard, V., Koster, J., Colmet Daage, L., Diskin, S.J., Schild, L., Bentahar, N.B., Bellini, A., Chicard, M., et al. (2015). Relapsed neuroblastomas show frequent RAS-MAPK pathway mutations. *Nat. Genet.* 47, 864–871. <https://doi.org/10.1038/ng.3333>.
  10. Qiu, B., and Matthay, K.K. (2022). Advancing therapy for neuroblastoma. *Nat. Rev. Clin. Oncol.* 19, 515–533. <https://doi.org/10.1038/s41571-022-00643-z>.
  11. Wienke, J., Dierselhuis, M.P., Tytgat, G.A.M., Künkele, A., Nierkens, S., and Molenaar, J.J. (2021). The immune landscape of neuroblastoma: Challenges and opportunities for novel therapeutic strategies in pediatric oncology. *Eur. J. Cancer* 144, 123–150. <https://doi.org/10.1016/j.ejca.2020.11.014>.
  12. Voeller, J., and Sondel, P.M. (2019). Advances in Anti-GD2 Immunotherapy for Treatment of High-risk Neuroblastoma. *J. Pediatr. Hematol. Oncol.* 41, 163–169. <https://doi.org/10.1097/MPH.0000000000001369>.
  13. Desai, A.V., Gilman, A.L., Ozkaynak, M.F., Naranjo, A., London, W.B., Tenney, S.C., Dicciani, M., Hank, J.A., Parisi, M.T., Shulkin, B.L., et al. (2022). Outcomes Following GD2-Directed Postconsolidation Therapy for Neuroblastoma After Cessation of Random Assignment on ANBL0032: A Report From the Children’s Oncology Group. *J. Clin. Oncol.* 40, 4107–4118. <https://doi.org/10.1200/JCO.21.02478>.
  14. Del Bufalo, F., De Angelis, B., Caruana, I., Del Baldo, G., De Ioris, M.A., Serra, A., Mastronuzzi, A., Cefalo, M.G., Pagliara, D., Amicucci, M., et al. (2023). GD2-CART01 for Relapsed or Refractory High-Risk Neuroblastoma. *N. Engl. J. Med.* 388, 1284–1295. <https://doi.org/10.1056/NEJMoa2210859>.
  15. Dong, R., Yang, R., Zhan, Y., Lai, H.-D., Ye, C.-J., Yao, X.-Y., Luo, W.-Q., Cheng, X.-M., Miao, J.-J., Wang, J.-F., et al. (2020). Single-Cell Characterization of Malignant Phenotypes and Developmental Trajectories of Adrenal Neuroblastoma. *Cancer Cell* 38, 716–733.e6. <https://doi.org/10.1016/j.ccell.2020.08.014>.
  16. Jansky, S., Sharma, A.K., Körber, V., Quintero, A., Toprak, U.H., Wecht, E.M., Gartlgruber, M., Greco, A., Chomsky, E., Grünwald, T.G.P., et al. (2021). Single-cell transcriptomic analyses provide insights into the developmental origins of neuroblastoma. *Nat. Genet.* 53, 683–693. <https://doi.org/10.1038/s41588-021-00806-1>.
  17. Kildisiute, G., Kholosy, W.M., Young, M.D., Roberts, K., Elementaite, R., van Hooff, S.R., Pacyna, C.N., Khabirova, E., Piapi, A., Thevanesan, C., et al. (2021). Tumor to normal single-cell mRNA comparisons reveal a pan-neuroblastoma cancer cell. *Sci. Adv.* 7, eabd3311. <https://doi.org/10.1126/sciadv.abd3311>.
  18. Costa, A., Thirant, C., Kramdi, A., Pierre-Eugène, C., Louis-Brennetot, C., Blanchard, O., Surdez, D., Gruel, N., Lapouble, E., Pierron, G., et al. (2022). Single-cell transcriptomics reveals shared immunosuppressive landscapes of mouse and human neuroblastoma. *J. Immunother. Cancer* 10, e004807. <https://doi.org/10.1136/jitc-2022-004807>.
  19. Slyper, M., Porter, C.B.M., Ashenberg, O., Waldman, J., Drokhylyansky, E., Wakiro, I., Smillie, C., Smith-Rosario, G., Wu, J., Dionne, D., et al. (2020). A single-cell and single-nucleus RNA-Seq toolbox for fresh and frozen human tumors. *Nat. Med.* 26, 792–802. <https://doi.org/10.1038/s41591-020-0844-1>.
  20. Verhoeven, B.M., Mei, S., Olsen, T.K., Gustafsson, K., Valind, A., Lindström, A., Gisselsson, D., Fard, S.S., Hagerling, C., Kharchenko, P.V., et al. (2022). The immune cell atlas of human neuroblastoma. *Cell Rep. Med.* 3, 100657. <https://doi.org/10.1016/j.xcrm.2022.100657>.
  21. Yuan, X., Seneviratne, J.A., Du, S., Xu, Y., Chen, Y., Jin, Q., Jin, X., Balachandran, A., Huang, S., Xu, Y., et al. (2022). Single-cell profiling of peripheral neuroblastic tumors identifies an aggressive transitional state that bridges an adrenergic-mesenchymal trajectory. *Cell Rep.* 41, 111455. <https://doi.org/10.1016/j.celrep.2022.111455>.
  22. Bedoya-Reina, O.C., Li, W., Arceo, M., Plescher, M., Bullova, P., Pui, H., Kaucka, M., Kharchenko, P., Martinsson, T., Holmberg, J., et al. (2021). Single-nuclei transcriptomes from human adrenal gland reveal distinct cellular identities of low and high-risk neuroblastoma tumors. *Nat. Commun.* 12, 5309. <https://doi.org/10.1038/s41467-021-24870-7>.
  23. Thirant, C., Peltier, A., Durand, S., Kramdi, A., Louis-Brennetot, C., Pierre-Eugène, C., Gautier, M., Costa, A., Grelier, A., Zaïdi, S., et al. (2023). Reversible transitions between noradrenergic and mesenchymal tumor identities define cell plasticity in neuroblastoma. *Nat. Commun.* 14, 2575. <https://doi.org/10.1038/s41467-023-38239-5>.
  24. Gautier, M., Thirant, C., Delattre, O., and Janoueix-Lerosey, I. (2021). Plasticity in Neuroblastoma Cell Identity Defines a Noradrenergic-to-Mesenchymal Transition (NMT). *Cancers* 13, 2904. <https://doi.org/10.3390/cancers13122904>.
  25. Bedoya-Reina, O.C., and Schlisio, S. (2021). Chromaffin Cells with Sympathoblast Signature: Too Similar to Keep Apart? *Cancer Cell* 39, 134–135. <https://doi.org/10.1016/j.ccell.2020.12.009>.
  26. Kameneva, P., Artemov, A.V., Kastriiti, M.E., Faure, L., Olsen, T.K., Otte, J., Erickson, A., Semsch, B., Andersson, E.R., Ratz, M., et al. (2021). Single-cell transcriptomics of human embryos identifies multiple sympathoblast lineages with potential implications for neuroblastoma origin. *Nat. Genet.* 53, 694–706. <https://doi.org/10.1038/s41588-021-00818-x>.
  27. Kildisiute, G., Young, M.D., and Behjati, S. (2021). Pitfalls of Applying Mouse Markers to Human Adrenal Medullary Cells. *Cancer Cell* 39, 132–133. <https://doi.org/10.1016/j.ccell.2020.12.006>.
  28. Williams, M., and Scott, C.L. (2022). Liver macrophages in health and disease. *Immunity* 55, 1515–1529. <https://doi.org/10.1016/j.immuni.2022.08.002>.
  29. Novella-Rausell, C., Grudniewska, M., Peters, D.J.M., and Mahfouz, A. (2023). A comprehensive mouse kidney atlas enables rare cell population characterization and robust marker discovery. *iScience* 26, 106877. <https://doi.org/10.1016/j.isci.2023.106877>.
  30. Lotfollahi, M., Naghipourfar, M., Luecken, M.D., Khajavi, M., Büttner, M., Wagenstetter, M., Avsec, Ž., Gayoso, A., Yosef, N., Interlandi, M., et al. (2022). Mapping single-cell data to reference atlases by transfer learning. *Nat. Biotechnol.* 40, 121–130. <https://doi.org/10.1038/s41587-021-01001-7>.
  31. Salcher, S., Sturm, G., Horvath, L., Untergasser, G., Kuempers, C., Fotakis, G., Panizzolo, E., Martowicz, A., Trebo, M., Pall, G., et al. (2022). High-resolution single-cell atlas reveals diversity and plasticity of tissue-resident neutrophils in non-small cell lung cancer. *Cancer Cell* 40, 1503–1520.e8. <https://doi.org/10.1016/j.ccell.2022.10.008>.
  32. Sikkema, L., Ramírez-Suástegui, C., Strobl, D.C., Gillett, T.E., Zappia, L., Madisson, E., Markov, N.S., Zaragosi, L.-E., Ji, Y., Ansari, M., et al. (2023). An integrated cell atlas of the lung in health and disease. *Nat. Med.* 29, 1563–1577. <https://doi.org/10.1038/s41591-023-02327-2>.
  33. Oh, K., Yoo, Y.J., Torre-Healy, L.A., Rao, M., Fassler, D., Wang, P., Caponegro, M., Gao, M., Kim, J., Sasson, A., et al. (2023). Coordinated single-cell tumor microenvironment dynamics reinforce pancreatic cancer subtype. *Nat. Commun.* 14, 5226. <https://doi.org/10.1038/s41467-023-40895-6>.
  34. Gayoso, A., Lopez, R., Xing, G., Boyeau, P., Valiollah Pour Amiri, V., Hong, J., Wu, K., Jayasuriya, M., Mehlman, E., Langevin, M., et al. (2022). A Python library for probabilistic analysis of single-cell omics

- data. *Nat. Biotechnol.* **40**, 163–166. <https://doi.org/10.1038/s41587-021-01206-w>.
35. Lopez, R., Regier, J., Cole, M.B., Jordan, M.I., and Yosef, N. (2018). Deep generative modeling for single-cell transcriptomics. *Nat. Methods* **15**, 1053–1058. <https://doi.org/10.1038/s41592-018-0229-2>.
  36. Korsunsky, I., Millard, N., Fan, J., Slowikowski, K., Zhang, F., Wei, K., Baglaenko, Y., Brenner, M., Loh, P.R., and Raychaudhuri, S. (2019). Fast, sensitive and accurate integration of single-cell data with Harmony. *Nat. Methods* **16**, 1289–1296. <https://doi.org/10.1038/s41592-019-0619-0>.
  37. Tirosh, I., Izar, B., Prakadan, S.M., Wadsworth, M.H., Treacy, D., Trombetta, J.J., Rotem, A., Rodman, C., Lian, C., Murphy, G., et al. (2016). Dissecting the multicellular ecosystem of metastatic melanoma by single-cell RNA-seq. *Science* **352**, 189–196. <https://doi.org/10.1126/science.aad0501>.
  38. De Falco, A., Caruso, F., Su, X.-D., Iavarone, A., and Ceccarelli, M. (2023). A variational algorithm to detect the clonal copy number substructure of tumors from scRNA-seq data. *Nat. Commun.* **14**, 1074. <https://doi.org/10.1038/s41467-023-36790-9>.
  39. van Groningen, T., Koster, J., Valentijn, L.J., Zwijnenburg, D.A., Akogul, N., Hasselt, N.E., Broekmans, M., Haneveld, F., Nowakowska, N.E., Bras, J., et al. (2017). Neuroblastoma is composed of two super-enhancer-associated differentiation states. *Nat. Genet.* **49**, 1261–1266. <https://doi.org/10.1038/ng.3899>.
  40. Boeva, V., Louis-Brennetot, C., Peltier, A., Durand, S., Pierre-Eugène, C., Raynal, V., Etchevers, H.C., Thomas, S., Lermine, A., Daudigeos-Dubus, E., et al. (2017). Heterogeneity of neuroblastoma cell identity defined by transcriptional circuitries. *Nat. Genet.* **49**, 1408–1413. <https://doi.org/10.1038/ng.3921>.
  41. Gartgruber, M., Sharma, A.K., Quintero, A., Dreidax, D., Jansky, S., Park, Y.-G., Kretsch, S., Meder, J., Doncevic, D., Saary, P., et al. (2021). Super enhancers define regulatory subtypes and cell identity in neuroblastoma. *Nat. Cancer* **2**, 114–128. <https://doi.org/10.1038/s43018-020-00145-w>.
  42. Mañas, A., Aaltonen, K., Andersson, N., Hansson, K., Adamska, A., Seger, A., Yasui, H., van den Bos, H., Radke, K., Esfandyari, J., et al. (2022). Clinically relevant treatment of PDX models reveals patterns of neuroblastoma chemoresistance. *Sci. Adv.* **8**, eabq4617. <https://doi.org/10.1126/sciadv.abq4617>.
  43. Takahashi, N., Kim, S., Schultz, C.W., Rajapakse, V.N., Zhang, Y., Redon, C.E., Fu, H., Pongor, L., Kumar, S., Pommier, Y., et al. (2022). Replication stress defines distinct molecular subtypes across cancers. *Cancer Res. Commun.* **2**, 503–517. <https://doi.org/10.1158/2767-9764.crc-22-0168>.
  44. Blosser, W.D., Dempsey, J.A., McNulty, A.M., Rao, X., Ebert, P.J., Lowery, C.D., Iversen, P.W., Webster, Y.W., Donoho, G.P., Gong, X., et al. (2020). A pan-cancer transcriptome analysis identifies replication fork and innate immunity genes as modifiers of response to the CHK1 inhibitor prexasertib. *Oncotarget* **11**, 216–236. <https://doi.org/10.18632/oncotarget.27400>.
  45. Van Haver, S., Fan, Y., Bekaert, S.-L., Everaert, C., Van Looche, W., Zanzani, V., Deschildre, J., Maestre, I.F., Amaro, A., Vermeirssen, V., et al. (2024). Human iPSC modeling recapitulates in vivo sympathoadrenal development and reveals an aberrant developmental subpopulation in familial neuroblastoma. *iScience* **27**, 108096. <https://doi.org/10.1016/j.isci.2023.108096>.
  46. Fischer, M., Grossmann, P., Padi, M., and DeCaprio, J.A. (2016). Integration of TP53, DREAM, MMB-FOXO1 and RB-E2F target gene analyses identifies cell cycle gene regulatory networks. *Nucleic Acids Res.* **44**, 6070–6086. <https://doi.org/10.1093/nar/gkw523>.
  47. Gavish, A., Tyler, M., Greenwald, A.C., Hoefflin, R., Simkin, D., Tschernichovsky, R., Gallili Darnell, N., Somech, E., Barbolin, C., Antman, T., et al. (2023). Hallmarks of transcriptional intratumour heterogeneity across a thousand tumours. *Nature* **618**, 598–606. <https://doi.org/10.1038/s41586-023-06130-4>.
  48. Rajbhandari, P., Lopez, G., Capdevila, C., Salvatori, B., Yu, J., Rodriguez-Barrueco, R., Martinez, D., Yarmarkovich, M., Weichert-Leahey, N., Abraham, B.J., et al. (2018). Cross-Cohort Analysis Identifies a TEAD4-MYCN Positive Feedback Loop as the Core Regulatory Element of High-Risk Neuroblastoma. *Cancer Discov.* **8**, 582–599. <https://doi.org/10.1158/2159-8290.CD-16-0861>.
  49. Lu, F., Mu, B., Jin, G., Zhu, L., and Mu, P. (2022). MYCN Directly Targets NeuroD1 to Promote Cellular Proliferation in Neuroblastoma. *Oncol. Res.* **29**, 1–10. <https://doi.org/10.37277/096504021X16401852341873>.
  50. Chen, L., Alexe, G., Dharia, N.V., Ross, L., Iniguez, A.B., Conway, A.S., Wang, E.J., Veschi, V., Lam, N., Qi, J., et al. (2018). CRISPR-Cas9 screen reveals a MYCN-amplified neuroblastoma dependency on EZH2. *J. Clin. Invest.* **128**, 446–462. <https://doi.org/10.1172/JCI90793>.
  51. Brodeur, G.M., Nakagawara, A., Yamashiro, D.J., Ikegaki, N., Liu, X.-G., Azar, C.G., Lee, C.P., and Evans, A.E. (1997). Expression of TrkA, TrkB and TrkC in human neuroblastomas. *J. Neuro Oncol.* **31**, 49–55. <https://doi.org/10.1023/A:1005729329526>.
  52. Zhang, Y., Du, Y., Wang, M., Li, C., Zhao, Z., Peng, L., Zhou, J., and Wang, S. (2023). Identification of genes associated with spontaneous regression of neuroblastoma. *Pediatr. Discov.* **7**, e10. <https://doi.org/10.1002/pdi3.10>.
  53. Fabian, J., Opitz, D., Althoff, K., Lodrini, M., Hero, B., Volland, R., Beckers, A., de Preter, K., Decock, A., Patil, N., et al. (2016). MYCN and HDAC5 transcriptionally repress CD9 to trigger invasion and metastasis in neuroblastoma. *Oncotarget* **7**, 66344–66359. <https://doi.org/10.18632/oncotarget.11662>.
  54. Kang, W., Hu, J., Zhao, Q., and Song, F. (2021). Identification of an Autophagy-Related Risk Signature Correlates With Immunophenotype and Predicts Immune Checkpoint Blockade Efficacy of Neuroblastoma. *Front. Cell Dev. Biol.* **9**, 731380. <https://doi.org/10.3389/fcell.2021.731380>.
  55. Albers, A.R., O'Dorisio, M.S., Balster, D.A., Caprara, M., Gosh, P., Chen, F., Hoeger, C., Rivier, J., Wenger, G.D., O'Dorisio, T.M., and Qualman, S.J. (2000). Somatostatin receptor gene expression in neuroblastoma. *Regul. Pept.* **88**, 61–73. [https://doi.org/10.1016/S0167-0115\(99\)00121-4](https://doi.org/10.1016/S0167-0115(99)00121-4).
  56. Heumos, L., Schaar, A.C., Lance, C., Litnitskaya, A., Drost, F., Zappia, L., Lücken, M.D., Strobl, D.C., Henao, J., Curion, F., et al. (2023). Best practices for single-cell analysis across modalities. *Nat. Rev. Genet.* **24**, 550–572. <https://doi.org/10.1038/s41576-023-00586-w>.
  57. Zeineldin, M., Patel, A.G., and Dyer, M.A. (2022). Neuroblastoma: When differentiation goes awry. *Neuron* **110**, 2916–2928. <https://doi.org/10.1016/j.neuron.2022.07.012>.
  58. Andreatta, M., and Carmona, S.J. (2021). UCell: Robust and scalable single-cell gene signature scoring. *Comput. Struct. Biotechnol. J.* **19**, 3796–3798. <https://doi.org/10.1016/j.csbj.2021.06.043>.
  59. Aibar, S., González-Blas, C.B., Moerman, T., Huynh-Thu, V.A., Imrichova, H., Hulselmans, G., Rambow, F., Marine, J.-C., Geurts, P., Aerts, J., et al. (2017). SCENIC: single-cell regulatory network inference and clustering. *Nat. Methods* **14**, 1083–1086. <https://doi.org/10.1038/nmeth.4463>.
  60. Chapple, R.H., Liu, X., Natarajan, S., Alexander, M.I.M., Kim, Y., Patel, A.G., LaFlamme, C.W., Pan, M., Wright, W.C., Lee, H.-M., et al. (2024). An integrated single-cell RNA-seq map of human neuroblastoma tumors and preclinical models uncovers divergent mesenchymal-like gene expression programs. *Genome Biol.* **25**, 161. <https://doi.org/10.1186/s13059-024-03309-4>.
  61. Lachmann, A., Xu, H., Krishnan, J., Berger, S.I., Mazloom, A.R., and Ma'ayan, A. (2010). ChEA: transcription factor regulation inferred from integrating genome-wide ChIP-X experiments. *Bioinformatics* **26**, 2438–2444. <https://doi.org/10.1093/bioinformatics/btq466>.
  62. Vanhauwaert, S., Decaestecker, B., De Brouwer, S., Leonelli, C., Durinck, K., Mestdagh, P., Vandessompele, J., Sermon, K., Denecker, G., Van Neste, C., et al. (2018). In silico discovery of a FOXM1 driven embryonal

- signaling pathway in therapy resistant neuroblastoma tumors. *Sci. Rep.* 8, 17468. <https://doi.org/10.1038/s41598-018-35868-5>.
63. Nunes, C., Depestel, L., Mus, L., Keller, K.M., Delhaye, L., Louwagie, A., Rishfi, M., Whale, A., Kara, N., Andrews, S.R., et al. (2022). RRM2 enhances MYCN-driven neuroblastoma formation and acts as a synergistic target with CHK1 inhibition. *Sci. Adv.* 8, eabn1382. <https://doi.org/10.1126/sciadv.abn1382>.
  64. Rishfi, M., Krols, S., Martens, F., Bekaert, S.-L., Sanders, E., Eggermont, A., De Vloed, F., Goulding, J.R., Risseuw, M., Molenaar, J., et al. (2023). Targeted AURKA degradation: Towards new therapeutic agents for neuroblastoma. *Eur. J. Med. Chem.* 247, 115033. <https://doi.org/10.1016/j.ejmech.2022.115033>.
  65. Nunes, C., Bekaert, S.-L., Parsa, S., Nelen, I., Martens, F., T'sas, S., Zhao, P., De Vloed, F., Eggermont, A., Goossens, S., et al. (2023). TPX2 as Key Downstream Target of the eIF4A Controlled Translational Program in MYCN Driven Neuroblastoma. Preprint at iScience. <https://doi.org/10.2139/ssrn.4551354>.
  66. van den Brink, S.C., Sage, F., Vétesy, Á., Spanjaard, B., Peterson-Maduro, J., Baron, C.S., Robin, C., and van Oudenaarden, A. (2017). Single-cell sequencing reveals dissociation-induced gene expression in tissue subpopulations. *Nat. Methods* 14, 935–936. <https://doi.org/10.1038/nmeth.4437>.
  67. SEQC/MAQC-III Consortium (2014). A comprehensive assessment of RNA-seq accuracy, reproducibility and information content by the Sequencing Quality Control Consortium. *Nat. Biotechnol.* 32, 903–914. <https://doi.org/10.1038/nbt.2957>.
  68. Louault, K., Porras, T., Lee, M.-H., Muthugounder, S., Kennedy, R.J., Blavier, L., Sarte, E., Fernandez, G.E., Yang, F., Pawel, B.R., et al. (2022). Fibroblasts and macrophages cooperate to create a pro-tumorigenic and immune resistant environment via activation of TGF- $\beta$ /IL-6 pathway in neuroblastoma. *Oncotarget* 11, 2146860. <https://doi.org/10.1080/2162402X.2022.2146860>.
  69. Williams, M., Bonnardel, J., Haest, B., Vanderborght, B., Wagner, C., Remmerie, A., Buijko, A., Martens, L., Thoné, T., Browaeys, R., et al. (2022). Spatial proteogenomics reveals distinct and evolutionarily conserved hepatic macrophage niches. *Cell* 185, 379–396.e38. <https://doi.org/10.1016/j.cell.2021.12.018>.
  70. Vitale, C., Bottino, C., and Castriconi, R. (2023). Monocyte and Macrophage in Neuroblastoma: Blocking Their Pro-Tumoral Functions and Strengthening Their Crosstalk with Natural Killer Cells. *Cells* 12, 885. <https://doi.org/10.3390/cells12060885>.
  71. Stip, M.C., Teeuwen, L., Dierselhuis, M.P., Leusen, J.H.W., and Krijgsman, D. (2023). Targeting the myeloid microenvironment in neuroblastoma. *J. Exp. Clin. Cancer Res.* 42, 337. <https://doi.org/10.1186/s13046-023-02913-9>.
  72. Williams, M., Dutertre, C.-A., Scott, C.L., McGovern, N., Sichien, D., Chakarov, S., Van Gassen, S., Chen, J., Poidinger, M., De Prijck, S., et al. (2016). Unsupervised High-Dimensional Analysis Aligns Dendritic Cells across Tissues and Species. *Immunity* 45, 669–684. <https://doi.org/10.1016/j.immuni.2016.08.015>.
  73. Kvedaraitė, E., and Ginhoux, F. (2022). Human dendritic cells in cancer. *Sci. Immunol.* 7, eabm9409. <https://doi.org/10.1126/sciimmunol.abm9409>.
  74. Liu, Z., Wang, H., Li, Z., Dress, R.J., Zhu, Y., Zhang, S., De Feo, D., Kong, W.T., Cai, P., Shin, A., et al. (2023). Dendritic cell type 3 arises from Ly6C<sup>+</sup> monocyte-dendritic cell progenitors. *Immunity* 56, 1761–1777.e6. <https://doi.org/10.1016/j.immuni.2023.07.001>.
  75. Dutertre, C.-A., Becht, E., Irac, S.E., Khalilnezhad, A., Narang, V., Khalilnezhad, S., Ng, P.Y., van den Hoogen, L.L., Leong, J.Y., Lee, B., et al. (2019). Single-Cell Analysis of Human Mononuclear Phagocytes Reveals Subset-Defining Markers and Identifies Circulating Inflammatory Dendritic Cells. *Immunity* 51, 573–589.e8. <https://doi.org/10.1016/j.immuni.2019.08.008>.
  76. Bourdely, P., Anselmi, G., Vaivode, K., Ramos, R.N., Missolo-Koussou, Y., Hidalgo, S., Tosselo, J., Nuñez, N., Richer, W., Vincent-Salomon, A., et al. (2020). Transcriptional and Functional Analysis of CD1c<sup>+</sup> Human Dendritic Cells Identifies a CD163<sup>+</sup> Subset Priming CD8<sup>+</sup>CD103<sup>+</sup> T Cells. *Immunity* 53, 335–352.e8. <https://doi.org/10.1016/j.immuni.2020.06.002>.
  77. Cytlak, U., Resteu, A., Pagan, S., Green, K., Milne, P., Maisuria, S., McDonald, D., Hulme, G., Filby, A., Carpenter, B., et al. (2020). Differential IRF8 Transcription Factor Requirement Defines Two Pathways of Dendritic Cell Development in Humans. *Immunity* 53, 353–370.e8. <https://doi.org/10.1016/j.immuni.2020.07.003>.
  78. Hegde, S., Leader, A.M., and Merad, M. (2021). MDSC: Markers, development, states, and unaddressed complexity. *Immunity* 54, 875–884. <https://doi.org/10.1016/j.immuni.2021.04.004>.
  79. Xu, W., Li, S., Li, M., Yang, X., Xie, S., Lin, L., Li, G., and Zhou, H. (2021). Targeted elimination of myeloid-derived suppressor cells via regulation of the STAT pathway alleviates tumor immunosuppression in neuroblastoma. *Immunol. Lett.* 240, 31–40. <https://doi.org/10.1016/j.imlet.2021.09.011>.
  80. Carlson, L.-M., Rasmuson, A., Idborg, H., Segerström, L., Jakobsson, P.-J., Sveinbjörnsson, B., and Kogner, P. (2013). Low-dose aspirin delays an inflammatory tumor progression in vivo in a transgenic mouse model of neuroblastoma. *Carcinogenesis* 34, 1081–1088. <https://doi.org/10.1093/carcin/bgt009>.
  81. Frosch, J., Leontari, I., and Anderson, J. (2021). Combined Effects of Myeloid Cells in the Neuroblastoma Tumor Microenvironment. *Cancers* 13, 1743. <https://doi.org/10.3390/cancers13071743>.
  82. Liu, K.X., and Joshi, S. (2020). “Re-educating” Tumor Associated Macrophages as a Novel Immunotherapy Strategy for Neuroblastoma. *Front. Immunol.* 11, 1947. <https://doi.org/10.3389/fimmu.2020.01947>.
  83. Remmerie, A., Martens, L., Thoné, T., Castoldi, A., Seurinck, R., Pavie, B., Roels, J., Vanneste, B., De Prijck, S., Vanhockerhout, M., et al. (2020). Osteopontin Expression Identifies a Subset of Recruited Macrophages Distinct from Kupffer Cells in the Fatty Liver. *Immunity* 53, 641–657.e14. <https://doi.org/10.1016/j.immuni.2020.08.004>.
  84. Jaitin, D.A., Adlung, L., Thaiss, C.A., Weiner, A., Li, B., Descamps, H., Lundgren, P., Blierot, C., Liu, Z., Deczkowska, A., et al. (2019). Lipid-Associated Macrophages Control Metabolic Homeostasis in a Trem2-Dependent Manner. *Cell* 178, 686–698.e14. <https://doi.org/10.1016/j.cell.2019.05.054>.
  85. Katzenelenbogen, Y., Sheban, F., Yalin, A., Yofe, I., Svetlichnyy, D., Jaitin, D.A., Bornstein, C., Moshe, A., Keren-Shaul, H., Cohen, M., et al. (2020). Coupled scRNA-Seq and Intracellular Protein Activity Reveal an Immunosuppressive Role of TREM2 in Cancer. *Cell* 182, 872–885.e19. <https://doi.org/10.1016/j.cell.2020.06.032>.
  86. Park, M.D., Reyes-Torres, I., LeBerichel, J., Hamon, P., LaMarche, N.M., Hegde, S., Belabed, M., Troncoso, L., Grout, J.A., Magen, A., et al. (2023). TREM2 macrophages drive NK cell paucity and dysfunction in lung cancer. *Nat. Immunol.* 24, 792–801. <https://doi.org/10.1038/s41590-023-01475-4>.
  87. Kirschenbaum, D., Xie, K., Ingelfinger, F., Katzenelenbogen, Y., Abadie, K., Look, T., Sheban, F., Phan, T.S., Li, B., Zwicky, P., et al. (2024). Time-resolved single-cell transcriptomics defines immune trajectories in glioblastoma. *Cell* 187, 149–165.e23. <https://doi.org/10.1016/j.cell.2023.11.032>.
  88. Yofe, I., Shami, T., Cohen, N., Landsberger, T., Sheban, F., Stoler-Barak, L., Yalin, A., Phan, T.S., Li, B., Monteran, L., et al. (2023). Spatial and Temporal Mapping of Breast Cancer Lung Metastases Identify TREM2 Macrophages as Regulators of the Metastatic Boundary. *Cancer Discov.* 13, 2610–2631. <https://doi.org/10.1158/2159-8290.CD-23-0299>.
  89. Nahrendorf, M., and Swirski, F.K. (2016). Abandoning M1/M2 for a Network Model of Macrophage Function. *Circ. Res.* 119, 414–417. <https://doi.org/10.1161/CIRCRESAHA.116.309194>.

90. Xue, J., Schmidt, S.V., Sander, J., Draffehn, A., Krebs, W., Quester, I., De Nardo, D., Gohel, T.D., Emde, M., Schmidleithner, L., et al. (2014). Transcriptome-Based Network Analysis Reveals a Spectrum Model of Human Macrophage Activation. *Immunity* 40, 274–288. <https://doi.org/10.1016/j.immuni.2014.01.006>.
91. Denisenko, E., Guo, B.B., Jones, M., Hou, R., de Kock, L., Lassmann, T., Poppe, D., Clément, O., Simmons, R.K., Lister, R., and Forrest, A.R.R. (2020). Systematic assessment of tissue dissociation and storage biases in single-cell and single-nucleus RNA-seq workflows. *Genome Biol.* 21, 130. <https://doi.org/10.1186/s13059-020-02048-6>.
92. Ding, J., Adiconis, X., Simmons, S.K., Kowalczyk, M.S., Hession, C.C., Marjanovic, N.D., Hughes, T.K., Wadsworth, M.H., Burks, T., Nguyen, L.T., et al. (2020). Systematic comparison of single-cell and single-nucleus RNA-sequencing methods. *Nat. Biotechnol.* 38, 737–746. <https://doi.org/10.1038/s41587-020-0465-8>.
93. Andrews, T.S., Atif, J., Liu, J.C., Perciani, C.T., Ma, X.Z., Thoeni, C., Slycer, M., Eraslan, G., Segerstolpe, A., Manuel, J., et al. (2022). Single-Cell, Single-Nucleus, and Spatial RNA Sequencing of the Human Liver Identifies Cholangiocyte and Mesenchymal Heterogeneity. *Hepatology. Commun.* 6, 821–840. <https://doi.org/10.1002/hep4.1854>.
94. Fetahu, I.S., Esser-Skala, W., Dnyansagar, R., Sindelar, S., Rifatbegovic, F., Bileck, A., Skos, L., Bozsaky, E., Lazic, D., Shaw, L., et al. (2023). Single-cell transcriptomics and epigenomics unravel the role of monocytes in neuroblastoma bone marrow metastasis. *Nat. Commun.* 14, 3620. <https://doi.org/10.1038/s41467-023-39210-0>.
95. Pozniak, J., Pedri, D., Landeloes, E., Van Herck, Y., Antoranz, A., Vanwynsberghe, L., Nowosad, A., Roda, N., Makhzami, S., Bervoets, G., et al. (2024). A TCF4-dependent gene regulatory network confers resistance to immunotherapy in melanoma. *Cell* 187, 166–183.e25. <https://doi.org/10.1016/j.cell.2023.11.037>.
96. Boon, K., Caron, H.N., van Asperen, R., Valentijn, L., Hermus, M.C., van Sluis, P., Roobeek, I., Weis, I., VouÛte, P.A., Schwab, M., and Versteeg, R. (2001). N-myc enhances the expression of a large set of genes functioning in ribosome biogenesis and protein synthesis. *EMBO J.* 20, 1383–1393. <https://doi.org/10.1093/emboj/20.6.1383>.
97. De Preter, K., Vandesompele, J., Heimann, P., Yigit, N., Beckman, S., Schramm, A., Eggert, A., Stallings, R.L., Benoit, Y., Renard, M., et al. (2006). Human fetal neuroblast and neuroblastoma transcriptome analysis confirms neuroblast origin and highlights neuroblastoma candidate genes. *Genome Biol.* 7, R84. <https://doi.org/10.1186/gb-2006-7-9-r84>.
98. Rohrer, H. (2021). Linking human sympathoadrenal development and neuroblastoma. *Nat. Genet.* 53, 593–594. <https://doi.org/10.1038/s41588-021-00845-8>.
99. Binnewies, M., Roberts, E.W., Kersten, K., Chan, V., Fearon, D.F., Merad, M., Coussens, L.M., Gaborilovich, D.I., Ostrand-Rosenberg, S., Hedrick, C.C., et al. (2018). Understanding the tumor immune microenvironment (TIME) for effective therapy. *Nat. Med.* 24, 541–550. <https://doi.org/10.1038/s41591-018-0014-x>.
100. Sadeghi Rad, H., Monkman, J., Warkiani, M.E., Ladwa, R., O’Byrne, K., Rezaei, N., and Kulasinghe, A. (2021). Understanding the tumor microenvironment for effective immunotherapy. *Med. Res. Rev.* 41, 1474–1498. <https://doi.org/10.1002/med.21765>.
101. Wculek, S.K., Cueto, F.J., Mujal, A.M., Melero, I., Krummel, M.F., and Sancho, D. (2020). Dendritic cells in cancer immunology and immunotherapy. *Nat. Rev. Immunol.* 20, 7–24. <https://doi.org/10.1038/s41577-019-0210-z>.
102. Murphy, T.L., and Murphy, K.M. (2022). Dendritic cells in cancer immunology. *Cell. Mol. Immunol.* 19, 3–13. <https://doi.org/10.1038/s41423-021-00741-5>.
103. Marciscano, A.E., and Anandasabapathy, N. (2021). The role of dendritic cells in cancer and anti-tumor immunity. *Semin. Immunol.* 52, 101481. <https://doi.org/10.1016/j.smim.2021.101481>.
104. Tai, Y., Chen, M., Wang, F., Fan, Y., Zhang, J., Cai, B., Yan, L., Luo, Y., and Li, Y. (2024). The role of dendritic cells in cancer immunity and therapeutic strategies. *Int. Immunopharmacol.* 128, 111548. <https://doi.org/10.1016/j.intimp.2024.111548>.
105. Fabre, T., Barron, A.M.S., Christensen, S.M., Asano, S., Bound, K., Lech, M.P., Wadsworth, M.H., Chen, X., Wang, C., Wang, J., et al. (2023). Identification of a broadly fibrogenic macrophage subset induced by type 3 inflammation. *Sci. Immunol.* 8, eadd8945. <https://doi.org/10.1126/sciimmunol.add8945>.
106. Silvin, A., Uderhardt, S., Piot, C., Da Mesquita, S., Yang, K., Geirsdottir, L., Mulder, K., Eyal, D., Liu, Z., Bridlance, C., et al. (2022). Dual ontogeny of disease-associated microglia and disease inflammatory macrophages in aging and neurodegeneration. *Immunity* 55, 1448–1465.e6. <https://doi.org/10.1016/j.immuni.2022.07.004>.
107. Deczkowska, A., Keren-Shaul, H., Weiner, A., Colonna, M., Schwartz, M., and Amit, I. (2018). Disease-Associated Microglia: A Universal Immune Sensor of Neurodegeneration. *Cell* 173, 1073–1081. <https://doi.org/10.1016/j.cell.2018.05.003>.
108. Jung, S.-H., Hwang, B.-H., Shin, S., Park, E.-H., Park, S.-H., Kim, C.W., Kim, E., Choo, E., Choi, I.J., Swirski, F.K., et al. (2022). Spatiotemporal dynamics of macrophage heterogeneity and a potential function of Trem2hi macrophages in infarcted hearts. *Nat. Commun.* 13, 4580. <https://doi.org/10.1038/s41467-022-32284-2>.
109. Zerneck, A., Erhard, F., Weinberger, T., Schulz, C., Ley, K., Saliba, A.-E., and Cochain, C. (2023). Integrated single-cell analysis-based classification of vascular mononuclear phagocytes in mouse and human atherosclerosis. *Cardiovasc. Res.* 119, 1676–1689. <https://doi.org/10.1093/cvr/cvac161>.
110. Upadhyay, A.A., Viox, E.G., Hoang, T.N., Boddapati, A.K., Pino, M., Lee, M.Y.-H., Corry, J., Strongin, Z., Cowan, D.A., Beagle, E.N., et al. (2023). TREM2+ and interstitial-like macrophages orchestrate airway inflammation in SARS-CoV-2 infection in rhesus macaques. *Nat. Commun.* 14, 1914. <https://doi.org/10.1038/s41467-023-37425-9>.
111. MacDonald, L., Alivernini, S., Toluoso, B., Elmesmari, A., Somma, D., Perniola, S., Paglionico, A., Petricca, L., Bosello, S.L., Carfi, A., et al. (2021). COVID-19 and RA share an SPP1 myeloid pathway that drives PD-L1+ neutrophils and CD14+ monocytes. *JCI Insight* 6, e147413. <https://doi.org/10.1172/jci.insight.147413>.
112. Ramachandran, P., Dobie, R., Wilson-Kanamori, J.R., Dora, E.F., Henderson, B.E.P., Luu, N.T., Portman, J.R., Matchett, K.P., Brice, M., Marwick, J.A., et al. (2019). Resolving the fibrotic niche of human liver cirrhosis at single-cell level. *Nature* 575, 512–518. <https://doi.org/10.1038/s41586-019-1631-3>.
113. Molgora, M., Liu, Y.A., Colonna, M., and Cella, M. (2023). TREM2: A new player in the tumor microenvironment. *Semin. Immunol.* 67, 101739. <https://doi.org/10.1016/j.smim.2023.101739>.
114. O’Flanagan, C.H., Campbell, K.R., Zhang, A.W., Kabeer, F., Lim, J.L.P., Biele, J., Eirew, P., Lai, D., McPherson, A., Kong, E., et al. (2019). Dissociation of solid tumor tissues with cold active protease for single-cell RNA-seq minimizes conserved collagenase-associated stress responses. *Genome Biol.* 20, 210. <https://doi.org/10.1186/s13059-019-1830-0>.
115. Wu, T., Hu, E., Xu, S., Chen, M., Guo, P., Dai, Z., Feng, T., Zhou, L., Tang, W., Zhan, L., et al. (2021). clusterProfiler 4.0: A universal enrichment tool for interpreting omics data. *Innovation* 2, 100141. <https://doi.org/10.1016/j.xinn.2021.100141>.
116. Gao, R., Bai, S., Henderson, Y.C., Lin, Y., Schalck, A., Yan, Y., Kumar, T., Hu, M., Sei, E., Davis, A., et al. (2021). Delineating copy number and clonal substructure in human tumors from single-cell transcriptomes. *Nat. Biotechnol.* 39, 599–608. <https://doi.org/10.1038/s41587-020-00795-2>.
117. Berg, M., Petoukhov, I., van den Ende, I., Meyer, K.B., Guryev, V., Vonk, J.M., Carpaij, O., Banchemo, M., Hendriks, R.W., van den Berge, M., and Nawijn, M.C. (2023). FastCAR: fast correction for ambient RNA to facilitate differential gene expression analysis in single-cell RNA-sequencing

- datasets. *BMC Genom.* 24, 722. <https://doi.org/10.1186/s12864-023-09822-3>.
118. Wolf, F.A., Angerer, P., and Theis, F.J. (2018). SCANPY: large-scale single-cell gene expression data analysis. *Genome Biol.* 19, 15. <https://doi.org/10.1186/s13059-017-1382-0>.
  119. Germain, P.-L., Lun, A., Garcia Meixide, C., Macnair, W., and Robinson, M.D. (2021). Doublet identification in single-cell sequencing data using scDbIFinder. *F1000Res.* 10, 979. <https://doi.org/10.12688/f1000research.73600.2>.
  120. Stuart, T., Butler, A., Hoffman, P., Hafemeister, C., Papalexi, E., Mauck, W.M., Hao, Y., Stoeckius, M., Smibert, P., and Satija, R. (2019). Comprehensive Integration of Single-Cell Data. *Cell* 177, 1888–1902.e21. <https://doi.org/10.1016/j.cell.2019.05.031>.
  121. Hao, Y., Hao, S., Andersen-Nissen, E., Mauck, W.M., Zheng, S., Butler, A., Lee, M.J., Wilk, A.J., Darby, C., Zager, M., et al. (2021). Integrated analysis of multimodal single-cell data. *Cell* 184, 3573–3587.e29. <https://doi.org/10.1016/j.cell.2021.04.048>.
  122. Aran, D., Looney, A.P., Liu, L., Wu, E., Fong, V., Hsu, A., Chak, S., Naikawadi, R.P., Wolters, P.J., Abate, A.R., et al. (2019). Reference-based analysis of lung single-cell sequencing reveals a transitional profibrotic macrophage. *Nat. Immunol.* 20, 163–172. <https://doi.org/10.1038/s41590-018-0276-y>.
  123. Oh, S., Abdelnabi, J., Al-Dulaimi, R., Aggarwal, A., Ramos, M., Davis, S., Riester, M., and Waldron, L. (2020). HGNCHELPER: identification and correction of invalid gene symbols for human and mouse. *F1000Res.* 9, 1493. <https://doi.org/10.12688/f1000research.28033.2>.
  124. Johnson, W.E., Li, C., and Rabinovic, A. (2007). Adjusting batch effects in microarray expression data using empirical Bayes methods. *Biostatistics* 8, 118–127. <https://doi.org/10.1093/biostatistics/kxj037>.
  125. Habib, N., Li, Y., Heidenreich, M., Swiech, L., Avraham-David, I., Trombetta, J.J., Hession, C., Zhang, F., and Regev, A. (2016). Div-Seq: Single-nucleus RNA-Seq reveals dynamics of rare adult newborn neurons. *Science* 353, 925–928. <https://doi.org/10.1126/science.aad7038>.
  126. Gayoso, A., Steier, Z., Lopez, R., Regier, J., Nazor, K.L., Streets, A., and Yosef, N. (2021). Joint probabilistic modeling of single-cell multi-omic data with totalVI. *Nat. Methods* 18, 272–282. <https://doi.org/10.1038/s41592-020-01050-x>.
  127. Xu, C., Lopez, R., Mehlman, E., Regier, J., Jordan, M.I., and Yosef, N. (2021). Probabilistic harmonization and annotation of single-cell transcriptomics data with deep generative models. *Mol. Syst. Biol.* 17, e9620. <https://doi.org/10.15252/msb.20209620>.
  128. Amezcua, R.A., Lun, A.T.L., Becht, E., Carey, V.J., Carpp, L.N., Geistlinger, L., Marini, F., Rue-Albrecht, K., Risso, D., Sonesson, C., et al. (2020). Orchestrating single-cell analysis with Bioconductor. *Nat. Methods* 17, 137–145. <https://doi.org/10.1038/s41592-019-0654-x>.

STAR★METHODS

KEY RESOURCES TABLE

REAGENT or RESOURCE	SOURCE	IDENTIFIER
<b>Biological samples</b>		
Pediatric patient tumor tissue	This paper, UZ Ghent	ss
<b>Chemicals, peptides, and recombinant proteins</b>		
b-mercaptoethanol	Sigma-Aldrich	Cat# M3148
Collagenase A	Sigma-Aldrich	Cat# 11088793001
DAPI	Invitrogen	Cat# D1306; RIDD: AB_2629482
DMSO	Fisher Scientific	Cat# 10103483
Dnase I	Sigma-Aldrich	Cat# 04 536 282 001
EDTA	Westburg	Cat# 51234
FcBlock 2.4G2	Bioceros	N/A
FCS	Merck Life Science	Cat# F0804
Fixable Viability due Live/Dead - eFluor780	eBioscience	Cat# 65-0865-18
RPMI 1640	Gibco	Cat# 52400-025
RBC lysis buffer	BioLegend	Cat# 420302
<b>Deposited data</b>		
Manuscript code	This study	<a href="https://github.com/VIBTOBilab/NBATlas_manuscript">https://github.com/VIBTOBilab/NBATlas_manuscript</a>
In-house data	This study	GEO: GSE253865
In-house data	This study	EGA: EGAD50000000328
NBATlas reference atlas data	This study	Mendeley Data: <a href="https://doi.org/10.17632/yhcf6787yp.1">https://doi.org/10.17632/yhcf6787yp.1</a>
NBATlas reference atlas visualization	This study	R2 platform: <a href="https://hgserver2.amc.nl/cgi-bin/r2/main.cgi?dscope=NBSCA&amp;option=about_dscope">https://hgserver2.amc.nl/cgi-bin/r2/main.cgi?dscope=NBSCA&amp;option=about_dscope</a>
NBATlas reference atlas visualization	This study	<a href="https://single-cell.be/nbatlas/">https://single-cell.be/nbatlas/</a>
<b>Software and algorithms</b>		
AUCell (v1.20.2)	Aibar et al. <sup>59</sup>	<a href="https://www.bioconductor.org/packages/release/bioc/html/AUCell.html">https://www.bioconductor.org/packages/release/bioc/html/AUCell.html</a>
CellRanger (v6.1.2)	10x Genomics	<a href="http://www.10xgenomics.com">http://www.10xgenomics.com</a>
ClusterProfiler (v4.4.4)	Wu et al. <sup>115</sup>	<a href="https://bioconductor.org/packages/release/bioc/html/clusterProfiler.html">https://bioconductor.org/packages/release/bioc/html/clusterProfiler.html</a>
CopyKAT (v1.1.0)	Gao et al. <sup>116</sup>	<a href="https://github.com/navinlabcode/copykat">https://github.com/navinlabcode/copykat</a>
FastCAR (v0.1.0)	Berg et al. <sup>117</sup>	<a href="https://github.com/LungCellAtlas/FastCAR">https://github.com/LungCellAtlas/FastCAR</a>
fgsea (v1.22.0)	ss	<a href="https://bioconductor.org/packages/release/bioc/html/fgsea.html">https://bioconductor.org/packages/release/bioc/html/fgsea.html</a>
ggplot2	ss	<a href="https://cran.r-project.org/web/packages/ggplot2/">https://cran.r-project.org/web/packages/ggplot2/</a>
Harmony (v0.1.0)	Korsunsky et al. <sup>36</sup>	<a href="https://github.com/immunogenomics/harmony">https://github.com/immunogenomics/harmony</a>
infercnvpy (v0.4.2)	ss	<a href="https://github.com/icbi-lab/infercnvpy">https://github.com/icbi-lab/infercnvpy</a>
NMF (v0.24.0)	ss	<a href="https://cran.r-project.org/web/packages/NMF">https://cran.r-project.org/web/packages/NMF</a>
scanpy (v1.8.1)	Wolf et al. <sup>118</sup>	<a href="https://github.com/scverse/scanpy">https://github.com/scverse/scanpy</a>
scDbfFinder (v1.10.0)	Germain et al. <sup>119</sup>	<a href="https://github.com/plger/scDbfFinder">https://github.com/plger/scDbfFinder</a>
SCEVAN (v1.0.1)	De Falco et al. <sup>38</sup>	<a href="https://github.com/AntonioDeFalco/SCEVAN">https://github.com/AntonioDeFalco/SCEVAN</a>
scvi-tools (v0.16.4)	Gayoso et al. <sup>34</sup>	<a href="https://github.com/scverse/scvi-tools">https://github.com/scverse/scvi-tools</a>
Seurat (v4.1.0)	Stuart et al., <sup>120</sup> Hao et al. <sup>121</sup>	<a href="https://github.com/satijalab/seurat">https://github.com/satijalab/seurat</a>
SingleR (v1.10.0)	Aran et al. <sup>122</sup>	<a href="https://github.com/dviraran/SingleR">https://github.com/dviraran/SingleR</a>
UCell (v2.0.1)	Andreatta et al. <sup>58</sup>	<a href="https://github.com/carmonalab/UCell">https://github.com/carmonalab/UCell</a>

(Continued on next page)

**Continued**

REAGENT or RESOURCE	SOURCE	IDENTIFIER
Other		
Dong et al. (2020) tumor dataset	Dong et al. <sup>15</sup>	GEO: GSE137804
Kildisiute et al. (2021) tumor dataset	Kildisiute et al. <sup>17</sup>	<a href="https://www.neuroblastomacellatlas.org/">https://www.neuroblastomacellatlas.org/</a>
Slyper et al. (2020) tumor dataset	Slyper et al. <sup>19</sup>	GEO: GSE140819
Verhoeven et al. (2022) tumor dataset	Verhoeven et al. <sup>20</sup>	GEO: GSE147766
Jansky et al. (2021) fetal adrenal medulla dataset	Jansky et al. <sup>16</sup>	<a href="https://adrenal.kitz-heidelberg.de/developmental_programs_NB_viz/">https://adrenal.kitz-heidelberg.de/developmental_programs_NB_viz/</a>
Van Haver et al. (2024) iPSC dataset	Van Haver et al. <sup>45</sup>	GEO: GSE211661
SEQC cohort dataset	SEQC consortium <sup>67</sup>	GEO: GSE62564
NRC cohort dataset	NRC consortium <sup>48</sup>	GEO: GSE85047

**EXPERIMENTAL MODEL AND SUBJECT PARTICIPANT DETAILS**

All neuroblastoma patient samples were collected as residual material after both diagnostic workups and after acquiring informed consent from the patient's guardian, in accordance with the Ethical Committee of UZ Ghent (EC number 2019/1428). For further details, see [Table S1](#).

**METHOD DETAILS**

**Processing of published data into the NBAtlas**

**Data collection**

For the construction of the NBAtlas, only samples confirmed to be human neuroblastoma samples (based on the clinical metadata provided) were included. Samples of ganglioneuroma, ganglioneuroblastoma, PDX, mouse, cell line, etc. were excluded. For one dataset (Dong et al. 2020<sup>15</sup>), raw sequencing files (FASTQs) were available and were processed into count tables using CellRanger (v6.1.2) aligned to GRCh38.99. FastCAR<sup>117</sup> (v0.1.0) was used to limit ambient RNA using the CellRanger web summary to determine the 'emptyDropletCutoff' (other parameters were default), as described in.<sup>69</sup> For the other datasets,<sup>16–20</sup> count tables were downloaded from data repositories (e.g., GEO) or sent by the corresponding author. If available, unfiltered count tables were preferred over filtered count tables.

**Patient metadata**

Metadata was collected from the different publications or provided by the original authors and compiled. For most samples, INSS or INRG stage, MYCN amplification status, CNA profile, etc. was available, as reported by the authors (see [Table S1](#)). For one sample (Verhoeven2022\_NB37), MYCN-amplification classification was based on an extremely high (>98<sup>th</sup> quantile) MYCN expression in a large number of tumor cells (as also discussed with the authors, personal communication).

**Risk classification**

Since studies included in the NBAtlas used different risk-classification systems (COG, NB2004, INRG or not mentioned which one), we uniformly revised the risk status for each sample. High-risk samples were distinguished from low/intermediate samples if they originated from a patient with INSS 4/INRGSS M, MYCN amplification, or a segmental CNA profile. The remaining samples (i.e., with another INSS/INRGSS class, no MYCN amplification, and no segmental CNA profile) were classified as low/intermediate-risk.

**Data quality control**

To filter out remaining low-quality cells, a homogeneous filter of minimally 200 genes, minimally 500 counts, and maximally 10% or 25% mitochondrial reads, for single-nucleus or single-cell samples, respectively, was applied. To filter out remaining doublets, the current best-performing method-scDblFinder (v1.10.0) was used<sup>56,119</sup> (run per sample with default parameters and cluster = 'seurat\_clusters'). Gene names from different datasets were updated and made unique using the R package HGNCHELPER (v0.8.1).<sup>123</sup> After merging the different datasets, genes with nonzero counts in minimally 10 cells were retained.

**Data integration**

After merging the count data of all samples, standard pre-processing, and normalization using the scanpy<sup>118</sup> (v1.8.1) pipeline was performed (the top 5000 highly variable genes were retained for further analyses). To correct for batch effects, the scVI algorithm<sup>35</sup> was used (scvi-tools python package v0.16.4, with 'sample' as the covariate, n\_layers = 2, encode\_covariates = True, use\_layer\_norm = 'both', use\_batch\_norm = 'none'). The scVI model was trained with 'max\_epochs = 500' (and early\_stopping = True). Thereafter, the latent representation provided by scVI was used as input to generate a UMAP (using scanpy.pp.neighbors with n\_pcs = 15 and n\_neighbors = 20, followed by scanpy.tl.umap with min\_dist = 0.6). Clustering was performed with scanpy.tl.leiden. Integration with Harmony<sup>36</sup> was also performed (with 'sample' as the covariate) and showed highly similar results in terms of cell clustering, however, the immune cells were not as clearly separated from the neuroendocrine cells and we therefore proceeded with the scVI integration results.

### Cell type annotation

Cell types were annotated using canonical markers and differentially expressed (DE) genes (as indicated in the dot plot in Figure 1D). A cluster of cells coming from samples with adrenal cortex cells (and a few liver cells, based on *ASGR1* and *ALB* expression), mainly from samples Slyper2020\_nucleus\_HTAPP-244-SMP-451\_TST and Jansky2021\_NB02, respectively, was annotated as ‘stromal other’. DE genes were calculated using the FindMarkers function (Seurat<sup>121</sup> v4.1.1 package) per cluster or cell type (with min.diff.pct = 0.3, logfc.threshold = 0.3). DE genes were ranked based on a specificity score, defined for each gene as the average log<sub>2</sub> fold-change multiplied by the percentage of cells in the cluster expressing this gene over the percentage expressed in other cells.

### Copy number inference

For inference of CNAs, all cell types except for potential CNA-bearing cells, i.e., neuroendocrine, fibroblast, and Schwann cells, were included as reference cells. Infercnvpy (v0.4.2) was used to infer CNAs from the normalized counts (with window\_size = 250 and step = 1). Genomic positions of the genes were annotated with infercnvpy.io.genomic\_position\_from\_gtf using the GENCODE v43 gene annotation. Cells were clustered according to CNA profiles (using infercnvpy.tl.pca, infercnvpy.pp.neighbors, and infercnvpy.tl.leiden with default parameters) and CNA scores (genome-wide) were calculated with infercnvpy.tl.cnv\_score (with default parameters). To calculate CNA scores for chromosomes or chromosome arms, the infercnvpy.tl.cnv\_score function was used after infercnvpy was rerun per study and results were merged to minimize batch effects.

To confirm the infercnvpy results, we also used CopyKAT (v1.1.0)<sup>116</sup> and SCEVAN (v1.0.1).<sup>38</sup> Classification of aneuploid/tumor vs. diploid/normal cells was performed on a per-sample basis to exclude potential batch effects at classification. As for infercnvpy, all cell types except for neuroendocrine, fibroblast, and Schwann cells were used as reference cells. Providing a good baseline reference has been shown to drastically improve the confident classification performance.<sup>116</sup> To ensure this, only samples with at least 100 reference cells were classified (other samples were labeled ‘not.run’).

### Reference-based mapping to normal sympathoadrenal development

Reference mapping of neuroendocrine cells to a fetal adrenal medulla dataset (from Jansky et al. 2021<sup>16</sup>) and human induced pluripotent stem cell (iPSC) model of sympathoadrenal development (from Van Haver et al. 2024<sup>45</sup>) was performed with SingleR<sup>122</sup> (v1.10.0, default parameters) based on Spearman correlation or Seurat (using the FindTransferAnchors and TransferData functions with default parameters). Log-normalized counts were used as input for both the reference and query data.

### Gene signature scoring

To calculate gene signature scores and to be able to compare different signatures in the same cells, the UCell<sup>58</sup> (v2.0.1) method was used. To calculate multiple UCell signature scores at once, the enrichR function (R escape package, v1.6.0) was used. Cell cycle phase assignment was performed using the CellCycleScoring function (Seurat v4.1.1 package).

## Tumor and immune zoom

### Tumor zoom

Neuroendocrine cells classified as aneuploid cells by CopyKAT were selected for the malignant tumor zoom. Integration was performed again after standard scanpy preprocessing as described above (now with updated top 5000 highly variable genes). scVI integration was performed with the same parameters as above. Leiden clustering was performed (with a resolution of 0.5). We also tried Harmony for integration (with sample alone or sample and assay as the covariate) but this provided insufficient integration of single-cells and single-nuclei (because of the assay-specific expression of the top genes used for integration). Furthermore, we tried correcting for cell cycle but this removed most DE genes indicating a loss of biological heterogeneity and we thus abandoned this approach. Seurat integration<sup>120</sup> of the samples was run with the RPCA algorithm. ComBat integration<sup>124</sup> was run with default parameters (using scanpy.pp.combat with ‘samples’ as batch key). DE genes were calculated as described above (with default cutoffs). Gene set enrichment analysis (GSEA) was performed per cluster using the fgsea R package (v1.22.0) with a ranking based on the specificity score for all genes (see above) with Reactome 2022 and ChEA2022 gene sets. Only GSEA results with an FDR below 0.1 were visualized.

### NMF program detection

Non-negative matrix factorization (NMF) programs in malignant cells were determined as described by Gavish et al.<sup>47</sup> To account for batch effects, NMF was run for each sample separately using the NMF R library (v0.24.0). Only samples with 10 malignant cells were considered, as recommended by Gavish et al.<sup>47</sup> Metaprograms (MPs) were determined by clustering the reoccurring NMF programs by Jaccard similarity. MP-defining genes (or signatures) were derived by selecting the top 50 most recurring genes per metaprogram. MPs were investigated to represent not just one study (dataset). This was not the case for any MP.

NMF overrepresentation analysis was performed using the enricher function (clusterProfiler<sup>115</sup> R package v4.4.4) with the following gene sets: Hallmark genesets, C6 genesets, Reactome downloaded from MSigDB (<https://www.gsea-msigdb.org/gsea/msigdb/>) as well as a collection of signatures from different studies.<sup>16,21,44,46,47,66</sup>

### Metaprogram survival analysis

Survival analysis of MP signatures was performed using the SEQC cohort bulk RNA-seq data ( $n = 498$  samples, GEO accession: GSE49710) and NRC cohort microarray data ( $n = 276$  samples, GEO accession: GSE85047). Kaplan-Meier curves were calculated using overall survival for high vs. low (log<sub>2</sub>) expression of the MP signatures (highest quartile cutoff) using the survival R package (v3.5-7) package.  $p$  values were calculated with a log-rank test.

### **Gene signature scoring**

The UCell (as described above) and AUCell (v1.20.2)<sup>59</sup> signature scoring was performed with default parameters. For the UCell van Groningen et al. mesenchymal gene signature, the threshold was determined manually based on the expression in immune cells (used as background). For AUCell, the threshold was determined automatically (with inspection of the thresholds).

### **Immune zoom**

Immune cell types (myeloid, B cell, plasma, pDC, T cell, and NK cell) were selected from the entire atlas and reintegrated using the same scVI-pipeline as described above. Clustering was performed with the Leiden algorithm (with a resolution of 1). Low-quality cells clustering separately and/or co-expressing markers of non-immune populations were removed. DE genes were calculated as described above with FindMarkers (with default cutoffs).

### **Monocyte/macrophage zoom**

Monocytes and macrophages were selected from the immune zoom for realignment across the samples. Given the reduced number of cells/nuclei ( $n = 14,860$ ) the integration was performed using Harmony (v0.1.0) instead of the scVI-pipeline.<sup>36,56</sup> Another round of quality control was performed here to eliminate remaining doublets or low-quality cells/nuclei. DE gene calculation was performed in the same way as for the immune zoom.

## **In-house generated single-cell and single-nucleus RNA-seq data**

### **Patient samples**

Samples were transported in RPMI and on ice where possible. Samples were either processed fresh or first viably frozen (in a solution of 10% DMSO, 50% FCS, and 40% RPMI) or snap-frozen (no medium) before proceeding to the isolation of single cells or nuclei.

### **Isolation of single neuroblastoma cells**

Single-cell isolation was performed as described in Guilliams et al. 2022.<sup>69</sup> In short, tumor specimens were minced into small pieces and digested into single-cell suspensions using 1 mg/mL Collagenase A (Sigma-Aldrich) and 10 U/mL DNase I (Sigma-Aldrich) in RPMI at 37°C for a maximum of 30 min with agitation until the tissue was digested. Next, cells were pelleted by centrifugation (5 min at 400 g). Red blood cell lysis was performed when required by incubating the cells with RBC lysis buffer (BioLegend) for 3 min followed by a wash step. For CITE-seq, an Fc receptor block 2.4G2 (Bioss) was added together with CITE-seq antibodies (BioLegend; antibody details described in Guilliams et al. 2022<sup>69</sup>). Following 20 min of incubation at 4°C, the cells were washed with PBS with 2% FCS and 2mM EDTA. For regular single-cell RNA-seq, this step was omitted. Cells were then stained with a live-dead discrimination dye (Live/Dead eFluor780, eBioscience) by incubating the cells for 15 min at 4°C followed by a wash step. Approximately 160,000 live cells were then FACS-purified per sample (using BD FACSAria III). After sorting, cells were pelleted by centrifugation at (5 min at 400 g).

### **Isolation of single neuroblastoma nuclei**

Nuclei were isolated from snap-frozen tumor tissue as described in Guilliams et al. 2022<sup>69</sup> and Habib et al. 2016.<sup>125</sup> Briefly, snap or viably frozen neuroblastoma tissues were dounce homogenized in a homogenization buffer. The homogenate was filtered over a 70  $\mu\text{m}$  cell strainer. Next, the nuclei were pelleted using a sucrose density gradient ultracentrifugation (7,700 rpm for 30 min at 4°C). After resuspension, nuclei were stained with DAPI (Invitrogen) and incubated for 5 min, and 100,000 to 400,000 intact nuclei were FACS-purified from remaining debris (using BD FACSAria III). Purified nuclei were pelleted by centrifugation, first for 3 min at 400 g and subsequently for 5 min at 600 g.

### **Single-cell or single-nucleus RNA-sequencing**

After centrifugation, cells or nuclei were resuspended in 18.5  $\mu\text{L}$  in PBS with 0.04% BSA. 2  $\mu\text{L}$  of this solution was used to calculate the concentration of cells or nuclei after flow cytometric counting. 20,000 cells or nuclei were loaded onto a Chromium (10X Genomics) controller. Single-cell or single-nucleus libraries were generated using the Chromium Single Cell 3 (V2 or V3) Reagent Kit according to the manufacturer's protocol. Libraries were sequenced using an Illumina NovaSeq 6000 sequencing platform.

### **Matching single-cell and single-nucleus RNA-sequencing data processing**

For matching single-cell and single-nucleus data generation, we used four parts from one tumor and split each part into two pieces for matching CITE-seq and single-nucleus RNA-seq with two technical replicates each (i.e., CITE-seq: Bonine2023\_cell\_CS202-209 and single-nucleus RNA-seq: Bonine2023\_nucleus\_CS210-217). Data processing of the matching single-cell and single-nucleus RNA-seq data was performed similarly to that described above, using CellRanger (for single-nucleus data processing, the option include-introns = T was added) and FastCAR. Cells with at least 200 and less than 8,000 genes, less than 60,000 counts, and less than 40% mitochondrial reads were kept. Additionally, when merging the data of different samples, only genes with counts for at least three cells were retained. Preprocessing was done using the standard pre-processing and normalization scanpy pipeline. Different single-nuclei samples and CITE-seq samples were integrated using the TotalVI model<sup>126</sup> (v0.6.7, using the top 4000 most highly variable genes, according to the workflow described on [scvi-tools.org](https://scvi-tools.org)). Subsequently, Louvain clustering was performed in the TotalVI latent space. The antibody (ADT) counts from CITE-seq data were further not considered. Clusters with a decreased number of genes, increased percentage of mitochondrial reads, and/or expressing markers of multiple cell types were removed. Cell-type annotation was performed as described above.

### **In-house data for mapping to the NBAtlas**

In-house single-cell and single-nucleus RNA-seq data from six patients, with one having matched data (see [Table S1](#)), was included for mapping to the NBAtlas. All samples were individually pre-processed and quality control was performed with the same procedure

as described above for the NBAtlas. Manual annotation was performed for each sample following log-normalization and UMAP generation (with a standard Seurat pipeline) using the top markers from the NBAtlas.

#### ***scArches data integration and cell type prediction***

For the integration of in-house data with the NBAtlas, the scANVI-scArches pipeline was used. To exploit the biological knowledge already embedded in the atlas as cell type annotation, the scVI model was first further trained on the cell type labels with scANVI<sup>127</sup> (scvi-tools package v0.16.4, with `n_layers = 4`, `max_epochs = 500`, `early_stopping = 'True'`). This was then used as input for scArches model training (v0.5.6, `max_epochs = 500`) of the query data. scANVI-scArches cell type prediction was performed with an uncertainty of 0.5 (as recommended by the authors<sup>30</sup>). To obtain an integrated atlas of the query and reference atlas, a UMAP was generated in the scArches latent space. After the scArches integration, another round of quality control was performed. A cluster of doublets (co-expressing markers of different cell types), remaining in the in-house data was removed.

#### ***SingleR cell type prediction***

SingleR<sup>122</sup> (v1.10.0) cell type prediction of in-house data with the NBAtlas as a reference was run as described above (with default parameters). Ribosomal and mitochondrial genes were removed from the reference to avoid these being selected as genes for mapping. For visualization of the results of the query together with the reference data, we used the scArches UMAP.

#### **Visualization**

UMAPs were plotted with the Seurat (v4.1.1) or plot1cell (v0.0.1) package. Feature plots were created using ordered normalized expression using the FeaturePlot function (Seurat package) with a quantile cutoff of 0.02–0.98. Dot plots were generated with the DotPlot function (Seurat package) or with ggplot2. Other figures were created with ggplot2. Some icons were generated with Biorender.

#### **QUANTIFICATION AND STATISTICAL ANALYSIS**

For statistical comparison of means between two non-normally distributed unpaired conditions, the Wilcoxon test was used. Differential abundance testing was performed with the edgeR package (glmQLFTest function).<sup>128</sup> For correlation analysis, Kendall's rank correlation test was used. For survival analysis, the log rank test was used. For multiple testing, Benjamini-Hochberg correction was used.